

Fast, systematic and robust relative binding free energies for simple and complex transformations : dual-LAO

Narjes Ansari^{▽,*,†} Félix Aviat^{▽,*,†} Jérôme Hénin,[‡] Jean-Philip Piquemal,^{†,¶} and Louis Lagardère^{*,†,¶}

[†]*Qubit Pharmaceuticals, Advanced Research Department, 75014 Paris, France*

[‡]*Laboratoire de Biochimie Théorique, UPR 9080 CNRS, Université de Paris Cité, 75005 Paris, France*

[¶]*Laboratoire de Chimie Théorique, Sorbonne Université, UMR 7616 CNRS, 75005 Paris, France*

E-mail: narjesa@qubit-pharmaceuticals.com; felix.aviat@qubit-pharmaceuticals.com;
louis.lagardere@sorbonne-universite.fr

▀ N.A. and F.A. contributed equally.

Abstract

Relative Binding Free Energy (RBFE) calculations are a cornerstone of rational hit-to-lead and lead optimization in modern drug discovery. However, the high computational cost and limited reliability in tackling large or complex molecular transformations often prevent their routine, high-throughput use. Here we introduce dual-LAO, a novel, highly efficient method for calculating RBFE. Building on the Lambda-ABF-OPES framework, this method combines a dual-topology setup and suitable restraints to dramatically accelerate free energy convergence. We demonstrate that dual-LAO, in combination with the AMOEBA polarizable force field, achieves an unprecedented acceleration factor of 15 to 30 times compared to current state-of-the-art methods on standard drug targets. Crucially, the approach maintains high accuracy and successfully tackles previously prohibitive molecular changes, including scaffold-hopping, buried water displacement, charge changes, ring-opening, and binding pose perturbations. This significant leap in efficiency allows for the widespread, routine integration of predictive molecular simulations into the rapid optimization cycles of drug discovery, enabling chemists to confidently model historically challenging systems in timescales compatible with real-world project deadlines.

Introduction

Accelerating therapeutic development critically hinges on accurately predicting the binding affinity (ΔG) between small molecules and macromolecular targets.¹ Computational methods play a pivotal role, offering the potential to streamline the costly and time-consuming process of drug discovery by prioritizing promising candidates for experimental investigation.²⁻⁴ Among the most rigorous computational tools are physics-based alchemical free energy (AFE) methods, which leverage statistical mechanics and molecular simulations.⁵ Alchemical methods rely on the exploration of non-physical intermediate states to perform

a transformation between two physical end-states.

One class of such methods, Absolute Binding Free Energy (ABFE) calculations, aims to compute the total free energy change upon ligand binding.⁶ While conceptually appealing, ABFE prediction remains computationally demanding, often struggling with slow convergence due to the extensive conformational sampling required for both the binding process and the large alchemical transformations involved (e.g., full ligand decoupling).⁷ Achieving reliable ABFE results necessitates both accurate force fields capable of capturing subtle molecular interactions (including polarization)⁸ and highly efficient sampling techniques to overcome significant free energy barriers.^{9–18}

Consequently, RBFE calculations have become the predominant approach in hit-to-lead and lead optimization campaigns.¹⁹ RBFE methods calculate the difference in binding affinity ($\Delta\Delta G$) between two structurally related ligands (L_1 and L_2) via a thermodynamic cycle^{20,21} by alchemically transforming L_1 into L_2 in both the protein-bound state ($\Delta G_{complex}$) and the unbound, solvated state (ΔG_{solv}):

$$\Delta\Delta G = \Delta G_{complex} - \Delta G_{solv} \quad (1)$$

These methods benefit from significant error cancellation and typically involve smaller, more manageable perturbations than ABFEs.¹⁹ This makes RBFE less computationally intensive than ABFE and often capable of higher precision for comparing congeneric series.¹⁹ Furthermore, the computational cost for all these simulations has been dramatically reduced by the use of Graphics Processing Units (GPUs), enabling RBFE calculations to be performed with sufficient throughput to impact active drug discovery projects.¹⁹

The alchemical transformations in RBFE are typically performed using molecular dynamics (MD) simulations. The free energy difference is commonly estimated using methods like Free Energy Perturbation (FEP)²² or Thermodynamic Integration (TI),²³ often involving multiple simulations at discrete intermediate states along the transformation path. To im-

prove efficiency, alternative approaches have been developed. These include nonequilibrium methods,²⁴ as well as expanded ensemble techniques where the alchemical coupling parameter λ is treated as an extended variable that evolves during a single simulation. Prominent examples of the latter include λ -dynamics (λ D)²⁵ and its extension, multiple topology λ -Dynamics (MS λ D).²⁶ MS λ D is particularly scalable, allowing simultaneous perturbations at multiple molecular sites and enabling the exploration of large combinatorial chemical spaces with significantly fewer simulations than traditional FEP or TI.

To practically model this alchemical transformation, several topology schemes can be employed. The *single-topology* approach requires mapping the atoms of L_1 onto L_2 and introducing “dummy” atoms for non-matching regions, which can become complex for dissimilar ligands.^{20,27} The *dual-topology* approach simulates both L_1 and L_2 simultaneously, with the interactions of one ligand being “turned off” while the other is “turned on”.^{20,28} This avoids dummy atoms but can require careful spatial restraints to manage the non-interacting components.²⁹ An alternative is the *hybrid* or *modified dual-topology* scheme, which defines a maximal common substructure (MCS) as a single, shared entity while treating the non-shared “appearing” and “disappearing” regions separately, thus avoiding both dummy atoms and the need for complex restraints.^{30,31}

Modern RBFE protocols, combining advanced force fields (e.g., OPLS3e³²), enhanced sampling techniques (e.g., REST2³³), and automated workflows,¹⁹ have demonstrated impressive performance in numerous retrospective and prospective studies, frequently reporting root-mean-square errors (RMSE) relative to experiment approaching 1 kcal/mol.^{34–36} This level of accuracy, often designated as “chemical accuracy”, allows RBFE predictions to effectively rank compounds and guide synthesis prioritization.³⁴ Large-scale prospective studies have confirmed the value of RBFE in enriching hit rates for potent compounds compared to other methods.³⁷

Despite these successes, RBFE methods face significant challenges that can impact their reliability and accuracy.^{5,38} Accuracy is intrinsically limited by the underlying force field

and, critically, by the extent of conformational sampling. Insufficient sampling is a frequent pitfall, exacerbated by the chaotic nature of molecular dynamics, which mandates the use of ensemble simulations for statistically robust and reproducible results. Furthermore, the resulting free energy distributions are often non-Gaussian, complicating error analysis. Several specific scenarios are notoriously difficult: transformations involving large structural rearrangements (macrocyclization, scaffold hopping), changes in ligand net charge, covalent inhibitors, uncertainties in the initial binding pose, and perturbations involving the displacement or reorganization of buried water molecules. Ambiguities in protein structure (e.g., missing loops) also pose challenges, often necessitating retrospective validation before prospective use. It is also crucial to contextualize computational accuracy targets against experimental reproducibility limits; independent experimental measurements of the same affinity can differ by 0.8 – 1.0 kcal/mol ($\text{RMSE} \approx 0.6$ to $0.7 \text{ } pK_i$ units), setting a practical limit on achievable computational accuracy.

Recently, the Lambda-ABF-OPES method was introduced as a highly efficient hybrid approach for calculating ABFE.³⁹ By coupling Lambda-adaptive biasing force (Lambda-ABF) with On-the-fly Probability Enhanced Sampling (OPES), this technique achieves significantly faster convergence — up to 9-fold improvement compared to the original Lambda-ABF — while maintaining high accuracy, demonstrated with a mean absolute error of approximately 0.9 kcal/mol for challenging bromodomain inhibitors.³⁹ Lambda-ABF-OPES uses several simultaneous simulations called “walkers” regularly sharing information, effectively multiplying the exploration rate of the method. A key aspect contributing to the accuracy reached in this work is the use of the advanced AMOEBA polarizable force field.³⁹ Given the established difficulties in sampling for both ABFE and RBFE, applying such a demonstrably rapid and accurate methodology developed for ABFE within the RBFE context holds significant promise.

In this work, we introduce dual-LAO (Dual-topology, Dual-DBC Lambda-ABF-OPES), a novel RBFE strategy designed to significantly accelerate convergence and improve accu-

racy. This method integrates three core components: a dual-topology representation of the transformed ligands, enhanced alchemical sampling using the Lambda-ABF-OPES³⁹ framework, and a dual-DBC scheme utilizing specific distance-to-bound configuration (DBC) restraints. We implement this approach within the Tinker-HP simulation package, leveraging the advanced AMOEBA polarizable force field.⁴⁰ This combined approach benefits from the sampling power of Lambda-ABF-OPES, the flexibility of the dual topology method, and narrowing down of phase space volume due to the DBC restraints.

In the following, we rigorously evaluate the performance of this implementation across a spectrum of challenging scenarios frequently encountered in drug discovery. These transformations cover four distinct types, each posing unique challenges to sampling and convergence: (i) fragment-based transformations, including difficult charge-changing perturbations , (ii) perturbations involving problematic buried water displacement, (iii) fragment-like chemical perturbations, and (iv) complex scaffold-hopping perturbations, featuring challenging ring-opening transformations.

Our findings demonstrate the high accuracy and robustness of the dual-LAO method across this diverse and challenging set. Across the entire dataset comprising 30 compounds and 58 alchemical edges, the approach yields an overall edgewise RMSE of 0.51 kcal/mol and a pairwise RMSE of 0.56 kcal/mol, with a coefficient of determination (R^2) of 0.85. Crucially, this high level of accuracy is achieved with a simulation time of only 4 ns/walker for the complex and 2 ns/walker for the solvent phase per transformation (using 4 walkers). These results demonstrate that the dual-LAO approach consistently achieves rapid convergence and high accuracy, with RMSE values below 1 kcal/mol across all these RBFE test systems, in significantly smaller simulation time than conventional RBFE methods.

To further accelerate calculations, particularly when assessing multiple related analogues, we implemented Multiple topology dual-LAO within the Tinker-HP package. This extension allows for the simultaneous sampling of multiple alchemical transformations within a single simulation framework, leveraging the efficiency benefits observed in other multiple topology

dynamic lambda approaches.⁴¹ In this framework, all free energy differences are obtained concurrently from just one simulation run. As validation of this implementation, we calculated the relative hydration free energies for 15 distinct molecule pairs within the benzene family.

Methodology

The RBFE is calculated following eq. 1 (see Ref. 20 for the original thermodynamical cycle) which requires the computation of alchemical free energy components ($\Delta G_{complex}$ and ΔG_{Solv}). These components correspond to the transformation of a starting ligand (L_1) into a target ligand (L_2). Alchemical parameter λ is used to scale key interactions in the system's Hamiltonian such that $\lambda = 0$ corresponds to L_1 fully interacting and $\lambda = 1$ corresponds to L_2 fully interacting (with L_1 's intermolecular interactions fully deactivated).

Enhanced Alchemical Sampling: Dynamic λ and Lambda-ABF-OPES

In contrast to traditional techniques that utilize several simulations at fixed λ windows, this work treats λ as a dynamical variable coupled to the system through an extended Lagrangian scheme. The free energy difference (ΔG) is then obtained from the Potential of Mean Force (PMF) along λ . To ensure the required accuracy and rapid convergence, it is computed with the Lambda-ABF-OPES framework,³⁹ which combines:

- **Adaptive Biasing Force (ABF):** The Lambda-ABF scheme applies an adaptive biasing force to the fictitious particle λ . This force enables proper sampling of the λ space by flattening the free energy landscape along the alchemical path. The resulting PMF is then estimated using the TI estimator.
- **OPES-Explore (OPES_e) :** The Lambda-ABF scheme does not explicitly encompass capabilities to overcome energetic barriers orthogonal to the chosen collective

variable (λ). This is addressed by the addition of the exploratory version of the On-the-fly Probability Enhanced Sampling (OPES)^{16,17} method, known as OPES_e, a metadynamics-based method that aims at enhancing configurational sampling by lowering these orthogonal barriers.

This combination of efficient λ -space sampling from Lambda-ABF and enhanced exploration across orthogonal barriers (such as complex solvent or water exploration^{39,42}) from OPES_e constitutes the Lambda-ABF-OPES method.

Dual-Topology Scheme and Restraints

The transformation employs a dual-topology scheme^{20,28} where both ligands (L_1 and L_2) are simultaneously present. This approach simplifies input preparation (as no dummy atoms are required) and the computational cost of the extra atoms is negligible.

- **MCS Restraints:** The Maximal Common Substructure (MCS) is the substructure, common to both ligands, with the largest number of atoms or bonds. To ensure both ligands maintain a consistent conformation relative to their common parts, the MCS is identified using the FMCS algorithm,⁴³ and a set of dual-topology restraints (harmonic wall restraints) is applied to corresponding atoms in the MCS.
- **Binding Pose Restraints:** To prevent the ligand from escaping the binding pocket while its intermolecular interactions are scaled down, a dual-DBC scheme was implemented to positionally restrain the ligands, as detailed below.

Alchemical Schedule

The alchemical transformation from L_1 to L_2 is controlled using scaling factors for the intermolecular interactions (λ_{ELE}^X and λ_{VDW}^X). The continuous λ schedule is divided into three steps, as illustrated in Fig. 1 panel (a):

1. **Electrostatic Decoupling** ($\lambda = [0, 0.2]$): Electrostatic interactions of ligand L_1 are turned off by scaling down linearly its permanent multipoles and polarizability.
2. **VDW Switch** ($\lambda = [0.2, 0.8]$): Van-der-Waals interactions for L_1 are linearly turned off, and the same interactions for L_2 are linearly turned on.
3. **Electrostatic Coupling** ($\lambda = [0.8, 1.0]$): Electrostatic interactions of ligand L_2 are linearly activated by scaling up linearly its permanent multipoles and polarizabilities.

Dual DBC Restraint Scheme

To counteract positional drift during the intermediate λ states, we apply a flat-bottom harmonic restraint on the DBC of each ligand, using two independent, λ -dependent target distances, $\mathbf{d}_{\text{target}1}$ and $\mathbf{d}_{\text{target}2}$, as shown in Fig. 1(b).

The restraint acts only if the distance to DBC is higher than the target distance. The target distances are designed to have a minimum $D_{\min} = 2.0 \text{ \AA}$ and a maximum $D_{\max} = 10.0 \text{ \AA}$.

$$\mathbf{d}_{\text{target}1}(\lambda) = \begin{cases} D_{\min} & \text{for } \mathbf{0.0} \leq \lambda \leq \mathbf{0.9} \\ D_{\min} + \left(\frac{D_{\max} - D_{\min}}{2}\right) \left[1 - \cos\left(\frac{\pi(\lambda - 0.9)}{0.1}\right)\right] & \text{for } \mathbf{0.9} < \lambda \leq \mathbf{1.0} \end{cases} \quad (2)$$

$$\mathbf{d}_{\text{target}2}(\lambda) = \begin{cases} D_{\min} + \left(\frac{D_{\max} - D_{\min}}{2}\right) \left[1 + \cos\left(\frac{\pi\lambda}{0.1}\right)\right] & \text{for } \mathbf{0} \leq \lambda < \mathbf{0.1} \\ D_{\min} & \text{for } \mathbf{0.1} \leq \lambda \leq \mathbf{1.0} \end{cases} \quad (3)$$

Restraints are maintained at D_{\min} , but are gradually released near the end point corresponding to the decoupled ligand of interest by increasing the target distance to D_{\max} . As explained in a further section, the value of D_{\min} is chosen so that the binding mode of the fully coupled ligand of interest is not biased. This ensures that the final (fully coupled and fully decoupled) states are unbiased.

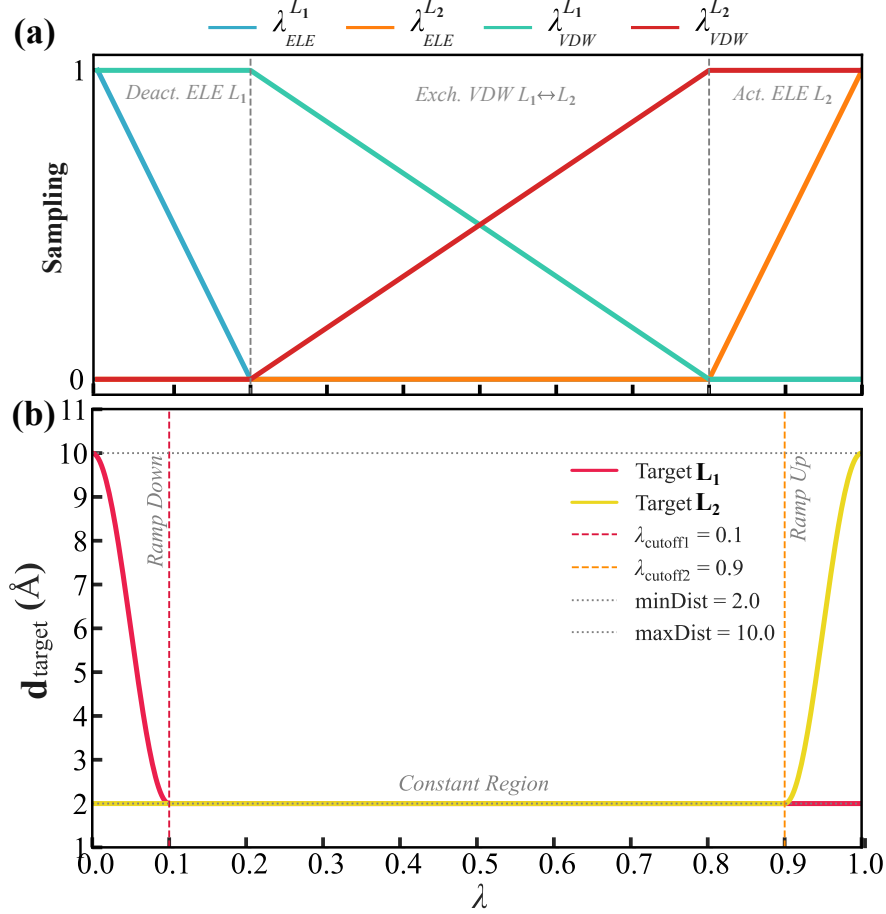


Figure 1: **Scaling of the intermolecular interactions and DBC restraint as a function of λ .** (a) Scaling of the intermolecular interactions for ligand L_1 ($\lambda_{ELE}^{L_1}$, $\lambda_{VDW}^{L_1}$) and ligand L_2 ($\lambda_{ELE}^{L_2}$, $\lambda_{VDW}^{L_2}$) as a function of λ . (b) Dual-DBC target distance profiles ($d_{\text{target}1}$ and $d_{\text{target}2}$) applied as harmonic positional restraints on the distance between centers (DBC) for complex alchemical transformations.

Implementation

The dual-LAO methodology was implemented within the Tinker-HP molecular dynamics software package,⁴⁰ leveraging the capabilities of the Colvars library⁴⁴ for managing the enhanced sampling Collective Variables and the specialized restraints.

Simulation Details

Plain MD Simulations

In this work, all molecular dynamics (MD) and advanced sampling simulations were performed using the Tinker-HP molecular dynamics package (Version 1.2),^{40,45} which includes the integrated `Colvars`⁴⁶ library for dual-LAO RBFE calculations. Simulations utilized the polarizable AMOEBA force field^{47–50} for the protein, solvent (water), and counter-ions. Ligand parameters were derived using the `Poltype` package.⁵¹ Each system was constructed within a cubic water box, sized to ensure a minimum separation of 12 Å between the ligand and any box boundary. The solvent was set to an aqueous NaCl solution at a concentration of 0.15 M to ensure physiological relevance and system neutrality.

A multi-stage protocol was employed to prepare the systems for production dynamics. First, the system underwent energy minimization via the Tinker-HP `minimize` utility, followed by a two-step heating phase from 200 K to 298 K under the NVT (canonical) ensemble. The first two steps utilized the RESPA integrator with a 2.0 fs time step: Step 1 (4 ns) involved applying positional restraints to all protein, ligand, and structural X-ray water atoms; in Step 2 (4 ns), these restraints were relaxed to act only on the heavy backbone atoms of the protein, maintained with a force constant of 10 kcal/mol/Å². Next, the system underwent a two-step relaxation phase. Step 3 (5 ns) involved further equilibration in the NVT ensemble using the three-level BAOAB-RESPA1 multiple-timestep integrator,⁵² where the outer time step was 10 fs, with intermediate and inner steps of 10/3 fs and 1 fs, respectively. For this step, restraints were applied only to C α atoms using a reduced force constant of 1 kcal/mol/Å². Finally, Step 4 (5 ns) conducted the final equilibration under the NPT (isothermal-isobaric) ensemble at 1 atm pressure, maintaining the C α restraints from the previous step. Following equilibration, a 20 ns production run was executed for each ligand complex in the NPT ensemble. The BAOAB-RESPA1 Langevin integrator was used with a 10 fs outer time step. Temperature control in non-Langevin steps was ensured by

the Bussi thermostat,⁵³ while pressure was regulated by the Berendsen barostat.⁵⁴ Van der Waals interactions employed a 12 Å cutoff. Electrostatic interactions were computed using the Particle Mesh Ewald (PME) method⁵⁵ with a 7 Å real-space cutoff. Induced dipoles were determined via a Preconditioned Conjugate Gradient (PCG) solver⁵⁶ to a convergence tolerance of 1×10^{-5} Debye.

dual-LAO Simulations

For all alchemical simulations, including R-group, buried water displacement, scaffold-hopping, and fragment-like transformations, we employed the dual-LAO method. We ran four walkers for each transformation, with 4 ns per walker for the complex phase and 2 ns per walker for the solvent phase. All other simulation parameters matched those of the plain MD simulations, with one exception: we used the BAOAB-RESPA integrator⁵² with a 2 fs time step.

DBC Selection

As described in Dual DBC Restraint Scheme section, we employed the DBC⁵⁷ to positionally restrain each L_1 and L_2 within its respective binding pose during complex alchemical transformations. The DBC coordinate quantifies the ligand’s deviation from its target pose by calculating the RMSD of a selected set of ligand atoms (noted LA) after optimal superposition onto a reference set of receptor binding site atoms (noted RB). This single variable efficiently captures positional, orientational, and conformational fluctuations of the ligand relative to its binding environment.

The selection of LA and RB atoms is crucial for defining a meaningful DBC restraint. To identify the least mobile parts of the ligand, we monitored the Root Mean Square Fluctuation (RMSF) of all heavy ligand atoms over a 20 ns conventional MD simulation of each individual complex. For the selection of the ligand atoms (LA) used in the DBC restraint, we applied a uniform Root Mean Square Fluctuation (RMSF) cutoff of 1.0 Å across all ligands and

targets under study. This ensures consistency in restraining the least flexible portions of the ligands undergoing alchemical coupling/decoupling. The RB set consisted of the $C\alpha$ atoms of the protein that fell within 6 Å of the ligand and exhibited an intrinsic flexibility below approximately 0.8 Å during the production MD.

To ensure that the DBC restraint does not introduce artificial bias during the alchemical simulation, we implemented a dual-DBC restraint strategy as explained earlier. Specifically, a minimum DBC value (DBC_{\min}) was set at 2 Å. This DBC_{\min} value was chosen to be lower than the upper bound of DBC coordinate value observed over the plain MD production run for each ligand, which was monitored using the Colvars library. A flat-bottomed harmonic restraint was applied to the DBC coordinate of both L_1 and L_2 during the dual-LAO simulations, following the DBC restraint schedule. This restraint employed a high force constant of 100 kcal/mol/Å² and was active only when the calculated DBC value exceeded the predetermined DBC cutoff.

Multiple Topology RBFs

The dual-topology framework is readily extensible to a multiple-topology framework (akin to the Separated Topologies Approach⁵⁸), which allows several alchemical transformations to be explored over the course of a single simulation. In a typical drug discovery campaign, the goal is to explore a network of transformations connecting a series of ligands (L_1, L_2, L_3, \dots). This network is defined by the user (e.g., using methods like LoMap⁵⁹) and is naturally represented as a graph. In this representation, each node denotes a molecule, and each edge represents the alchemical transformation between two connected molecules (not all pairs of molecules must be connected). Crucially, while the dual-topology framework explores each edge of this graph during an independent simulation, the multiple-topology framework allows all connected transformations to be explored during a single, extended simulation, following the procedure detailed below.

Any alchemical state of the multiple-topology simulation can be characterized with the

triplet (L_i, L_j, λ) , where L_i and L_j are the two molecules undergoing alchemical transformation, and λ , comprised in $[0; 1]$, describes the evolution of the transformation (as explained earlier)¹. If $\lambda = 0$, then L_i is fully coupled (and L_j fully decoupled), and if $\lambda = 1$, L_i is decoupled, L_j coupled.

The dual-LAO simulation is started on an (arbitrarily chosen) initial edge (L_i, L_j) of the graph. Just like in the dual-topology case, the value of λ is used to explore the alchemical schedule and define scaling terms for the VDW and ELE interactions of L_i and L_j , while all other ligands remain fully decoupled.

In the dual-topology scheme, the value of λ is kept within the $[0; 1]$ segment using reflexive boundary conditions. In the multiple-topology scheme, after applying reflexive boundary conditions, a special procedure is applied to enable exploration of other edges:

- (i) The node corresponding to the reflection value is identified.
- (ii) All edges connected to this node are identified.
- (iii) A random integer between 1 and the number of connected edges is drawn. This chooses the next edge of the network to explore, and defines a new triplet-state to explore.

This process allows the simulation to explore a new alchemical state whenever λ reaches (or exceeds) 0 or 1, which corresponds a “fully coupled” alchemical state.

Let us illustrate the process with an example: the simulation starts at $(L_1, L_2, \lambda = 0)$. After some time, λ reaches 1, which corresponds to the ligand L_2 being fully coupled. Let’s assume L_1, L_3, L_4 are connected to L_2 in our graph. A random integer is drawn between 1 and 3 (say, 2). This chooses the second connected edge to continue exploration, here L_2 to L_3 . The new triplet-state becomes $(L_3, L_2, \lambda = 1)$, and now alchemical transformation from L_2 to L_3 is explored.

With minimal extra input from the user (namely, the choice of a network via a connectivity matrix), this method allows to compute several RBFEs over the course of a single

¹Following this notation, the dual-topology case is simply described as the triplet (L_1, L_2, λ) .

simulation.

Results and Discussion

This section details the RBFE results obtained from various alchemical transformations using dual-LAO method. These transformations cover: fragment-based transformations, buried water displacement, fragment-like chemical perturbations, and scaffold-hopping perturbations. Representative examples are provided for each type.

RBFEs of Fragments for the PWWP1 Domain of NSD3

Our relative binding free energy RBFE simulations were performed as part of a fragment elaboration study targeting the PWWP1 domain of NSD3.⁶⁰ A set of 12 ligands (2D structures of the ligands are detailed in Fig. S2 of SI) was strategically selected,⁶¹ covering a significant range of binding affinities, specifically from an initial 160 μ M fragment hit (ligand 8) up to the highly potent 170 nM optimized lead compound, BI-9321. Detailed affinity data are provided in the Supporting Information Table S1. The alchemical free energy network for these transformations — primarily focused on R-group modifications — was initially constructed using the LoMap algorithm.⁵⁹ This yielded a total of 18 alchemical transformation pairs that connected the 12 ligands. These pairs were strategically chosen to represent different types of chemical changes and were broadly categorized into two types, as illustrated in Fig. 2 panels a₁ and a₂.

1. **Side Chain Transformations (Fig. 2 panel a₁):** These pairs feature two ligands that share the same central binding core (shown in yellow). The example of the transformation of ligand 10 to ligand 11 is shown in this figure, where the transformation occurs solely on a peripheral substituent. This type of transformation is typically less challenging to sample in RBFE calculations because the binding mode remains conserved.

2. Binding Pose Transformations (Fig. 2 panel a₂): These pairs represent a more challenging scenario in which the two ligands adopt different binding poses (for example ligand 17 to ligand 9466), leading to changes in protein-ligand interactions, including hydrogen bonding (HB) and van der Waals forces. This results in a binding free energy difference of around 3-4 kcal/mol. Such a substantial change in the protein-ligand interaction pattern and binding pose requires robust conformational sampling and presents a stringent test for the RBFE methodology.

In addition to the pose changes, the network included a charge transfer transformation (pair: lig10 → lig12, see Fig. S2). Such transformations, in which the charge state of a ligand changes between the initial and final states, are difficult to model accurately in the computational literature.³⁵ Our calculated result for this specific, challenging pair ($\Delta\Delta G_{\text{CAL}} = -1.22 \pm 0.11$ kcal/mol) shows excellent agreement with the experimental value ($\Delta\Delta G_{\text{EXP}} = -1.04$ kcal/mol). It is noteworthy that our results achieved convergence (see Figs. S4–S6) in less than 4 ns/walker for the complex phase and less than 2 ns/walker for the solvent phase. This contrasts sharply with state-of-the-art methods utilizing alchemical charge-changing perturbations, which typically require 24 λ windows, with each window simulated for 20 ns.³⁵ In total, for such challenging systems, our method demonstrates a convergence speed approximately 30 times faster.

To ensure statistical rigor of the calculations, RBFE was calculated in both directions ($L_1 \rightarrow L_2$ and $L_2 \rightarrow L_1$) for each pair, resulting in a total of 36 calculated relative free energy values ($\Delta\Delta G$) throughout the network (see Table S1).

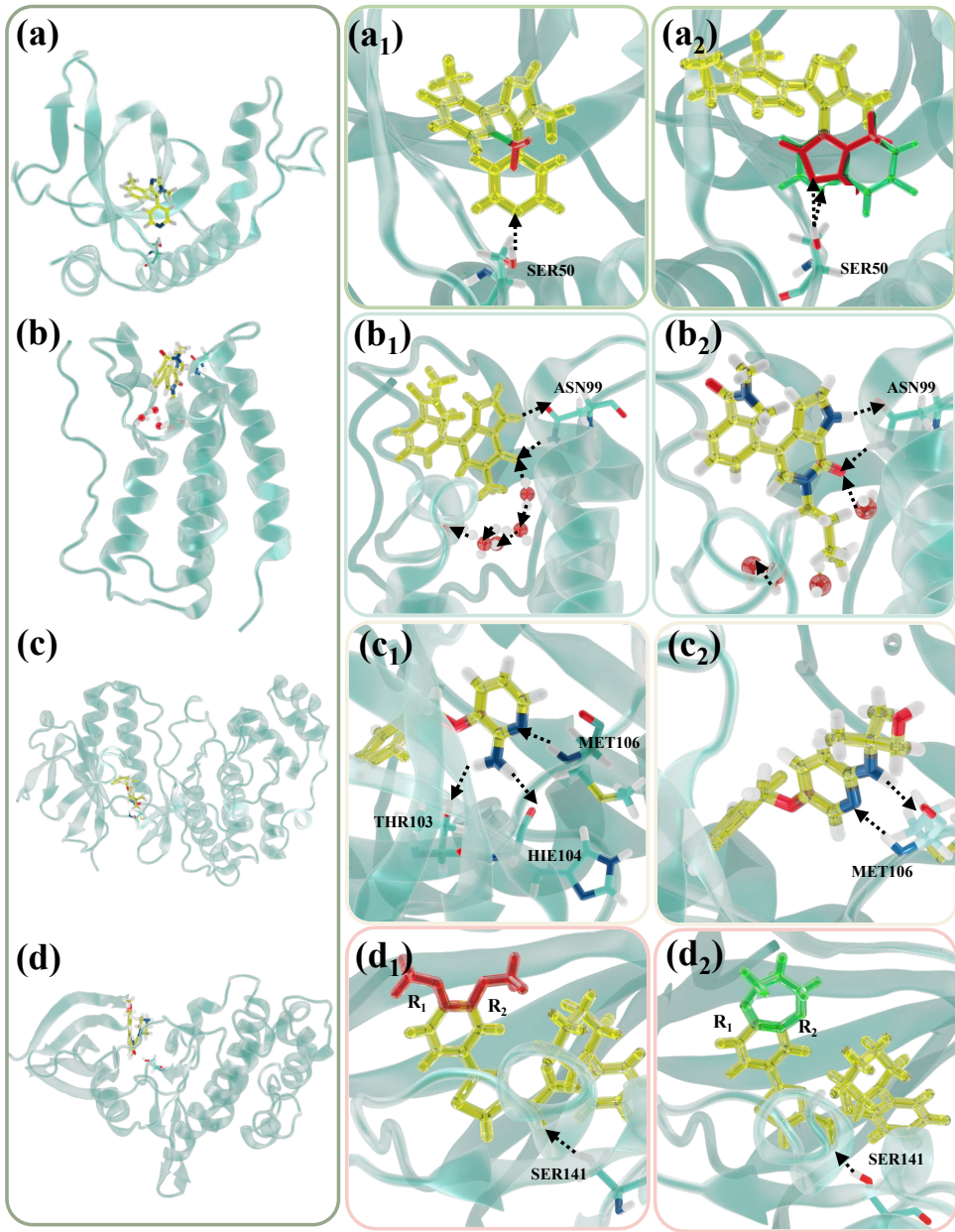


Figure 2: RBFE Alchemical Transformations and Systems. (a) PWWP1-ligand complex: (a₁) shows a side chain transformation where the change involves only the peripheral substituent, keeping the core binding pose conserved. (a₂) illustrates a binding pose transformation, where Ligand A (green) adopts a different pose compared to Ligand B (red), leading to new protein-ligand interactions. (b) BRD4-ligand complex: (b₁) and (b₂) display Buried Water Displacement. The comparison shows the displacement of ordered buried water molecules (red and white spheres) as the ligand size increases and extends its binding pose. (c) P38-ligand complex: (c₁) and (c₂) represent Fragment-Based Perturbations, where the transformation causes a change in the ligand's interaction with the protein. (d) CHK1-ligand complex: (d₁) and (d₂) show Scaffold-Hopping Transformations, where the R₁ and R₂ side chains change from an open form to a closed ring structure.

The calculations were performed using our dual topology framework and tested with the dual-DBC restraint scheme. The raw data, including the calculated $\Delta\Delta G$ and its associated uncertainty for every leg, are compiled in Table S1 in the Supporting Information.

The performance of the RBFE calculations was assessed by comparing the simulated values (noted $\Delta\Delta G$) with experimentally obtained ones (noted $\Delta\Delta G_{\text{EXP}}$). Fig. S1 (a) illustrates the correlation plot for the $\Delta\Delta G$ values, and Fig. 3(a) shows the correlation plot for the Absolute Binding Free Energy (ΔG) values derived from the relative network, following the method described in Supplementary Information.

The dual-DBC restraint scheme yielded excellent agreement with the experimental data, with the total RMSE for $\Delta\Delta G$ approximately 0.4 kcal/mol and RMSE of 0.63 kcal/mol for ΔG . This demonstrates the robustness of the methodology in different types of chemical transformations, including the pose changes and charge transfers.

RBFEs of BRD4 with Buried Water Displacement

One of the significant challenge in both ABFE and RBFE simulations arises when perturbations involve displacing buried water molecules within the protein active site.

To provide another challenging test for our current dual-LAO method, we thus selected the Bromodomain 4 (BRD4) system, as shown in Fig. 2 panels b₁ and b₂. This target is a well-known benchmark for computational methods, recognized to be problematic for achieving accurate binding free energies. In our prior studies^{39,42} utilizing the Lambda-ABF-OPES methodology, we successfully calculated the ABFE for seven targets with different variety of ligands featuring such buried water displacement events, and all results demonstrated excellent predictive accuracy for ΔG in these challenging systems. In the work by Ross et al.³⁵ using FEP+, the BRD4 ligand set presented considerable difficulty, resulting in an RMSE of 2.05 ± 0.24 kcal/mol and an R^2 value near zero.

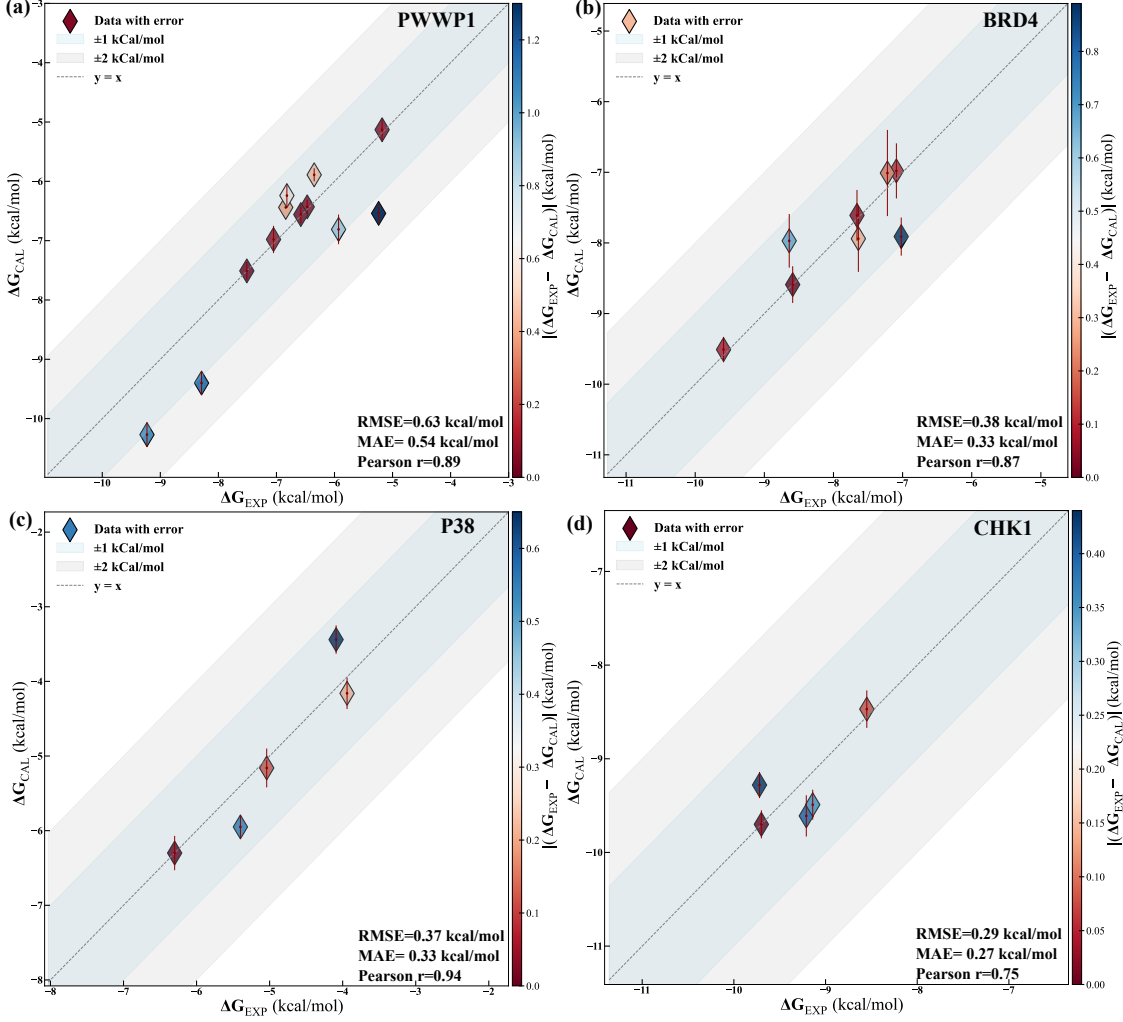


Figure 3: Experimental vs. Calculated Absolute Binding Free Energies (ΔG) derived from RBFE. (a) PWWP1, (b) BRD4, (c) P38, and (d) CHK1 complexes. The calculated ΔG results and associated errors represent the mean \pm standard error derived from the Weighted Least-Squares (WLS) fitting of the RBFE network (see SI for more details). The dark and light shaded regions indicate ± 1 kcal/mol and ± 2 kcal/mol deviations from the experimental values, respectively. The color bar displays the absolute difference between the experimental and computed values, $|\Delta G_{\text{EXP}} - \Delta G_{\text{CAL}}|$. For each system, key performance statistics including Pearson's r , RMSE, and MAE are reported.

We applied our dual-LAO approach to this same challenging set of ligands, which consists of eight ligands and eleven alchemical transformation pairs (see Fig. S7 for the 2D structures of the ligands). The correlation plots of $\Delta\Delta G$ and ΔG with experimental values are presented in S1b and 3b, respectively. Additionally, as an example, the convergence of PMF and the λ exploration over time for the transformation of ligand 2 (with six buried water molecules,

Fig. 2 panel b_1) to ligand 8 (with only four buried water molecules, Fig. 2 panel b_2) are shown in Figs. S9-S12. Here again, the convergence was achieved in less than 4 ns/walker for the complex phase and 2 ns/walker for the solvent phase.

dual-LAO results show a marked improvement over the FEP+ benchmark, demonstrating the method’s ability to handle systems involving complex buried water perturbations. Specifically, we achieved an RMSE of 0.60 kcal/mol and an R^2 of 0.75 for $\Delta\Delta G$, and an RMSE of 0.38 kcal/mol and an R^2 of 0.77 for ΔG .

In order to check the proper displacement of buried water molecules during the dual-LAO simulations, we analyzed as an example the coordination number (CN) of water around the O1 atom (see Fig. S8) for the alchemical transformation pair connecting ligand 2 ($\lambda = 0$) to ligand 5 ($\lambda = 1$). We focused specifically on this atom to ensure clear visualization and analysis of the water perturbation.

Fig. S8 displays the density plot of water molecules around the O1 atom as a function of the alchemical coupling parameter, λ . As shown in the figure, the coordination number of water molecules around the O1 atom is higher when the system is closer to the ligand 2 state ($\lambda \approx 0$) compared to the ligand 5 state ($\lambda \approx 1$). This difference confirms that the dual-LAO methodology successfully drives the necessary water perturbation and displacement as the ligand transforms.

RBFEs of P38 with fragment-like chemical perturbations

Fragment-like chemical perturbations represent a class of small, focused chemical modifications, often inspired by Fragment-Based Drug Discovery (FBDD), utilized in RBFE calculations. These perturbations typically involve subtle changes (e.g., adding a functional group or modifying a small ring) that connect highly similar ligands who share a conserved core binding motif.

We applied the dual-LAO method to the P38 fragment set from Ross et al.,³⁵ which comprises 5 ligands (See Fig. S13 for 2D structures of the ligands) and 7 transformations.

Panels c_1 and c_2 in fig. 2 show a representative transformation pair. Ligand 4 forms 3 stable hydrogen bonds (HBs) with residues THR103, HIE104, and MET106 (see Fig. 2 c_1), while Ligand 7 interacts only with residue MET106 via 2 HBs (see Fig. 2 c_2). In this specific perturbation, the left side of the two ligands is identical, while the right side undergoes a complex change.

For these transformations, our results yielded an RMSE of 0.37 kcal/mol for ABFE and 0.66 kcal/mol for RBFE. This excellent agreement further demonstrates the effectiveness of the dual-LAO method for accurately modeling such fragment-like transformations.

RBFEs of CHK1 with scaffold-hopping perturbations

As mentioned earlier, scaffold-hopping perturbations represent the most challenging and aggressive class of alchemical transformations studied using RBFE methods. Scaffold hopping involves replacing the core structural motif (the 'scaffold') of a ligand with a structurally distinct motif while aiming to retain similar potency and the overall binding mode.

To further challenge our method, we utilized the CHK1 scaffold-hopping set from Ross et al.³⁵ This set contains 5 ligands involved in 8 different transformations (the 2D structure of the ligands is available in Fig. S20. Fig. 2 panels d_1 and d_2 present one such transformation, where the CH_2CH_3 moiety in the R_1 and R_2 positions of Ligand 19 transforms into a closed 7-member ring in Ligand 21. This exemplifies a crucial ring opening/closing type of perturbation.

For this difficult transformation class, the dual-LAO method yielded an RMSE of 0.29 kcal/mol for ABFE and 0.52 kcal/mol for RBFE, indicating an excellent correlation between experimental and simulation results (see Fig. 2).

Table 1 and Fig. 4 collectively display the comprehensive performance of the dual-LAO method, covering the key statistics (R^2 and RMSE) across all four chemical systems, including both edgewise ($\Delta\Delta G$) and pairwise (ΔG) RMSE values.

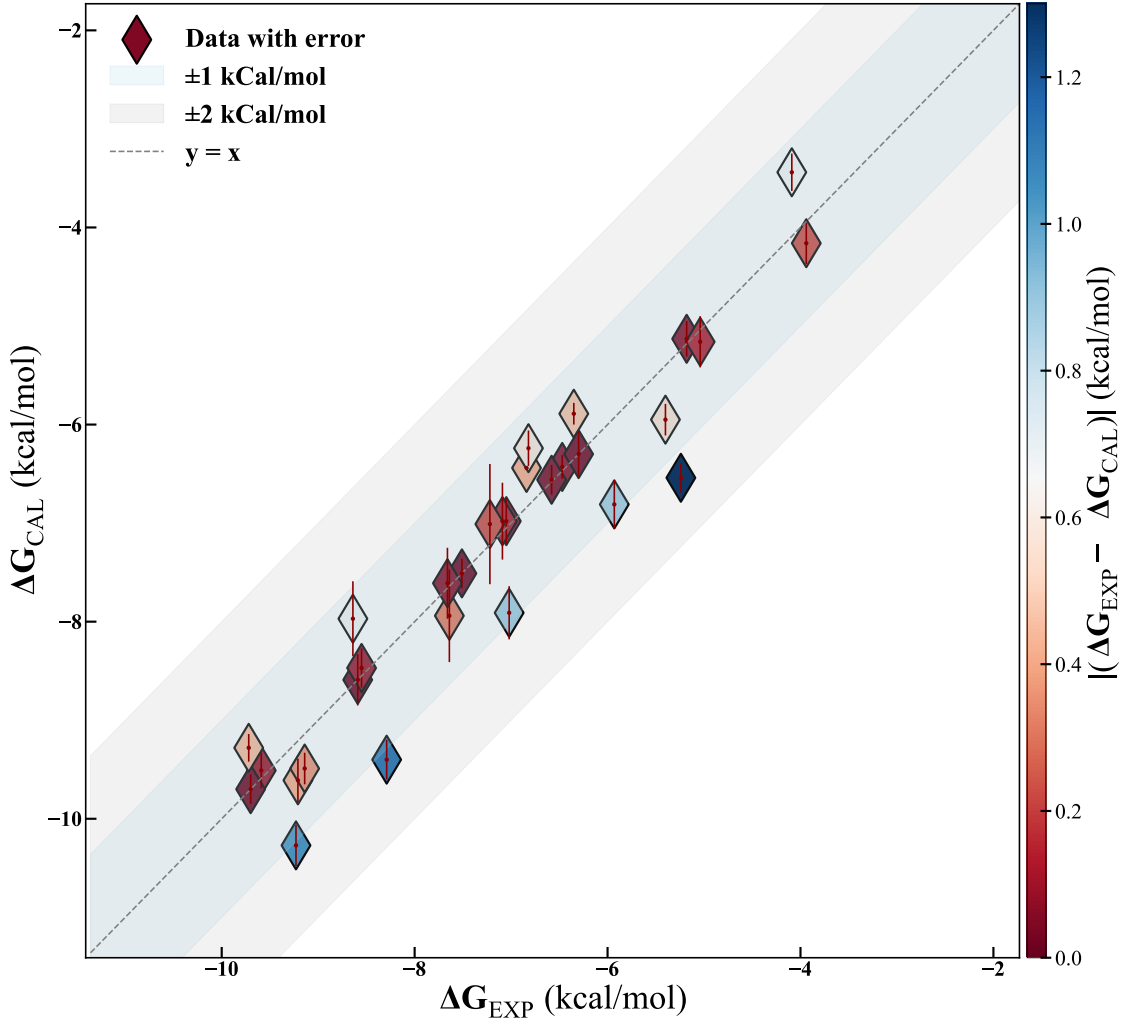


Figure 4: **Experimental vs. Calculated Absolute Binding Free Energies (ΔG) derived from the RBFE network fit for all studied systems.** The calculated ΔG results and associated errors represent the mean \pm standard error derived from the Weighted Least-Squares (WLS) fitting of the RBFE network. The dark and light shaded regions indicate ± 1 kcal/mol and ± 2 kcal/mol deviations from the experimental values, respectively. The color bar displays the absolute difference between the experimental and computed values, $|\Delta G_{EXP} - \Delta G_{CAL}|$.

Multi-site Hydration Free Energies for benzene derivatives

We applied our novel multiple-topology approach to the computation of Hydration Free Energies of six molecules deriving from benzene, as a proof of concept. Similarly to the difference in binding affinity as calculated in eq. (1), here the difference in hydration free energy

Table 1: Summary of RBFE Results for All Chemical Systems.

Performance statistics of the dual-LAO method compared to experimental data across all four chemical systems: PWWP1, BRD4, P38, and CHK1. The table includes the Protein Data Bank (PDB) identifier for the structure used, the total number of compounds and transformations (edges) in the set, the coefficient of determination (R^2) computed on $\Delta\Delta G$, and the RMSE calculated on both edgewise ($\Delta\Delta G$) and pairwise (ΔG) free energy differences. All RMSE values are given in kcal/mol.

System	PDB	No. compounds	No. edges	R^2	Edgewise RMSE	Pairwise RMSE
PWWP1	6G2B	12	32	0.92	0.63	0.43
BRD4	5I88	8	11	0.75	0.38	0.60
P38	1W7H	5	7	0.82	0.37	0.66
CHK1	3U9N	5	8	0.57	0.29	0.52
Total	-	30	58	0.85	0.51	0.56

is computed as the difference between the free energies associated to the transformation of L_1 into L_2 in the solvent phase and in vacuum, such that:

$$\Delta\Delta G_{\text{hydration}} = \Delta G_{\text{solv}} - \Delta G_{\text{gas}} \quad (4)$$

HFEs were computed on all fifteen possible pairs of molecules drawn from the chosen pool of six. Inputs were prepared by aligning molecules along the six carbons of the conjugated cycle. Multiple-topology transformations were explored over the course of 15 ns simulation.

As reference, HFEs were computed using the dual-topology method, with dual-LAO. For each transformation, simulations of 2 ns were used for the solvent phase alchemical transformation, and 1 ns for the molecule in vacuum. For all transformations (dual and multiple topology), three replicas were run.

A representation of the molecules (Fig. S23 as well as a comparison of the multi-site results with dual-site values (Fig. S24 are available in the Supplementary Information. Exploration of the expanded λ -space is shown in Fig. S25, and demonstrates the ability of the method to navigate throughout the various edges of the alchemical transformations graph. The RMSE (dual vs. multiple topology) for all RBFE values was 0.22 kcal/mol, and the Mean Average Error (MAE) 0.14 kcal/mol, with an excellent correlation coefficient R^2

of 0.997. This preliminary result indicates the fidelity of the λ -jumping scheme that was used. In future work, we plan to apply this method to Binding Free Energies and will assess in particular its potential gain in efficiency (we expect exploration to be enhanced by the jumps) and in accuracy (the explicit exploration of cycles during such simulations should help more rigorous cycle closure when compared to sequences of independent simulations).

Conclusion

We presented dual-LAO (Dual-topology, Dual-DBC Lambda-ABF-OPES), a new approach to compute relative free energies of binding that is built on a combination of Lambda-ABF-OPES for efficient sampling of the alchemical path, dual-topology for transformation flexibility, and dual-DBC restraints for optimal phase-space volume reduction. Used in conjunction with the AMOEBA polarizable force field, this strategy achieves chemical accuracy (overall RMSE of 0.51 kcal/mol) with a performance gain of more than an order of magnitude (over 15-fold acceleration) compared to state-of-the-art techniques. We demonstrated that the method is able to robustly tackle complex situations for which traditional approaches struggle. For example, we show that dual-LAO manages to reversibly rehydrate binding pockets upon ligand change (buried water displacement) without any specific tuning of the method. It also accurately handles other difficult perturbations including scaffold-hopping transformations, charge-changing, and ring-opening events with a marked improvement compared to state-of-the-art techniques. These advances make dual-LAO a robust and highly efficient tool to drive hit-to-lead and lead-optimization in drug discovery. The Multiple topology dual-LAO extension was successfully implemented and validated, confirming its potential for network-based RBFE evaluations. Future work will focus on the systematic study of the sampling improvement obtained thanks to the multi-site extension (especially regarding cycle-closure), as well as the application of dual-LAO to machine-learning foundation models such as FeNNix-Bio1.⁶²

Conflict of interest/Competing interests

L. L., and J.-P. P. are co-founders and shareholders of Qubit Pharmaceuticals. The remaining authors declare no competing interests.

Contributions

Designed research: L. L.; **Performed research:** N. A., F. A., L. L. ; **Performed simulations:** N. A., F. A. ; **Contributed analytic tools:** N. A., F. A.; **Contributed new code:** F. A., L. L.; **Analyzed data:** N. A., F. A., J. H., L. L., J.-P. P.; **Wrote the paper:** N. A., F. A., J. H., L. L., J.-P. P.

Acknowledgment

The authors would like to extend their gratitude to Oliver Adjoua and Florent Hédin for their unwavering support in all matters of code development, as well as Chengwen Liu for his help with AMOEBA parametrization.

This work was supported by computing grants from the Grand Équipement de Calcul Intensif (GENCI), Institut du Développement et des Ressources en Informatique (IDRIS), and Centre Informatique de l'Enseignement Supérieur (CINES), France, under grant numbers AD010715770 and AD010716167R1.

References

- (1) de Azevedo, J.; Walter, F.; Dias, R. Computational methods for calculation of ligand-binding affinity. *Curr. Drug Targets*. **2008**, 9, 1031–1039.
- (2) Jorgensen, W. L. Efficient Drug Lead Discovery and Optimization. *Accounts of Chemical Research* **2009**, 42, 724–733, PMID: 19317443.

(3) Homeyer, N.; Stoll, F.; Hillisch, A.; Gohlke, H. Binding Free Energy Calculations for Lead Optimization: Assessment of Their Accuracy in an Industrial Drug Design Context. 10, 3331–3344.

(4) Williams-Noonan, B. J.; Yuriev, E.; Chalmers, D. K. Free energy methods in drug design: prospects of “alchemical perturbation” in medicinal chemistry: miniperspective. J. Med. Chem. **2018**, 61, 638–649.

(5) Chodera, J. D.; Mobley, D. L.; Shirts, M. R.; Dixon, R. W.; Branson, K.; Pande, V. S. Alchemical free energy methods for drug discovery: progress and challenges. Current Opinion in Structural Biology **2011**, 21, 150–160.

(6) Song, L. F.; Merz, K. M. J. Evolution of Alchemical Free Energy Methods in Drug Discovery. Journal of Chemical Information and Modeling **2020**, 60, 5308–5318, PMID: 32818371.

(7) Gallicchio, E.; Levy, R. M. Advances in all atom sampling methods for modeling protein–ligand binding affinities. Current Opinion in Structural Biology **2011**, 21, 161–166.

(8) Amezcua, M.; El Khoury, L.; Mobley, D. L. SAMPL7 Host–Guest Challenge Overview: assessing the reliability of polarizable and non-polarizable methods for binding free energy calculations. 35, 1–35.

(9) Hénin, J.; Lelièvre, T.; Shirts, M. R.; Valsson, O.; Delemonette, L. Enhanced Sampling Methods for Molecular Dynamics Simulations [Article v1.0]. Living J. Comput. Mol. Sci. **2022**, 4, 1583.

(10) Torrie, G. M.; Valleau, J. P. Nonphysical sampling distributions in Monte Carlo free-energy estimation: Umbrella sampling. J. Comput. Phys. **1977**, 23, 187–199.

(11) Darve, E.; Pohorille, A. Calculating free energies using average force. J. Chem. Phys. **2001**, 115, 9169–9183.

(12) Darve, E.; Rodríguez-Gómez, D.; Pohorille, A. Adaptive biasing force method for scalar and vector free energy calculations. *J. Chem. Phys.* **2008**, 128, 144120–1.

(13) Comer, J.; Gumbart, J. C.; Hénin, J.; Lelièvre, T.; Pohorille, A.; Chipot, C. The adaptive biasing force method: Everything you always wanted to know but were afraid to ask. *J. Phys. Chem. B* **2015**, 119, 1129–1151.

(14) Laio, A.; Parrinello, M. Escaping free-energy minima. *Proc. Natl. Acad. Sci.* **2002**, 99, 12562–12566.

(15) Barducci, A.; Bonomi, M.; Parrinello, M. Metadynamics. *Wiley Interdiscip. Rev. Comput. Mol. Sci.* **2011**, 1, 826–843.

(16) Invernizzi, M.; Parrinello, M. Rethinking Metadynamics: From bias potentials to probability Distributions. *J. Phys. Chem. Lett.* **2020**, 11, 2731–2736.

(17) Invernizzi, M.; Parrinello, M. Exploration vs convergence speed in adaptive-bias enhanced sampling. *J. Chem. Theory Comput.* **2022**, 18, 3988–3996.

(18) Maragliano, L.; Vanden-Eijnden, E. A temperature accelerated method for sampling free energy and determining reaction pathways in rare events simulations. *Chem. Phys. Lett.* **2006**, 426, 168–175.

(19) Cournia, Z.; Allen, B.; Sherman, W. Relative Binding Free Energy Calculations in Drug Discovery: Recent Advances and Practical Considerations. *57*, 2911–2937.

(20) Pearlman, D. A.; Kollman, P. A. The overlooked bond-stretching contribution in free energy perturbation calculations. *94*, 4532–4545.

(21) York, D. M. Modern Alchemical Free Energy Methods for Drug Discovery Explained. *3*, 478–491.

(22) Zwanzig, R. W. High-temperature equation of state by a perturbation method. I. Non-polar gases. *J. Chem. Phys.* **1954**, 22, 1420–1426.

(23) Straatsma, T.; McCammon, J. Multiconfiguration thermodynamic integration. *J. Chem. Phys.* **1991**, 95, 1175–1188.

(24) Gapsys, V.; Seeliger, D.; de Groot, B. L. New Soft-Core Potential Function for Molecular Dynamics Based Alchemical Free Energy Calculations. *Journal of Chemical Theory and Computation* **2012**, 8, 2373–2382, PMID: 26588970.

(25) Kong, X.; Brooks, C. L. λ -dynamics: A new approach to free energy calculations. *J. Chem. Phys.* **1996**, 105, 2414–2423.

(26) Knight, J. L.; Brooks, C. L. I. Multisite λ Dynamics for Simulated Structure–Activity Relationship Studies. *Journal of Chemical Theory and Computation* **2011**, 7, 2728–2739, PMID: 22125476.

(27) Jorgensen, W. L.; Ravimohan, C. Monte simulation of differences in free energies of hydration. 83, 3050.

(28) Gao, J.; Kuczera, K.; Tidor, B.; Karplus, M. Hidden Thermodynamics of Mutant Proteins: A Molecular Dynamics Analysis. 244, 1069–1072.

(29) Ries, B.; Rieder, S.; Rhiner, C.; Hünenberger, P. H.; Riniker, S. RestraintMaker: a graph-based approach to select distance restraints in free-energy calculations with dual topology. 36, 175–192.

(30) Eriksson, M. A.; Nilsson, L. Structure, Thermodynamics and Cooperativity of the Glucocorticoid Receptor DNA-binding Domain in Complex with Different Response Elements. Molecular Dynamics Simulation and Free Energy Perturbation Studies. *Journal of Molecular Biology* **1995**, 253, 453–472.

(31) Jiang, W.; Chipot, C.; Roux, B. Computing Relative Binding Affinity of Ligands to Receptor: An Effective Hybrid Single-Dual-Topology Free-Energy Perturbation Approach

in NAMD. *Journal of Chemical Information and Modeling* **2019**, 59, 3794–3802, PMID: 31411473.

(32) Harder, E.; Damm, W.; Maple, J.; Wu, C.; Reboul, M.; Xiang, J. Y.; Wang, L.; Lupyan, D.; Dahlgren, M. K.; Knight, J. L. et al. OPLS3: A Force Field Providing Broad Coverage of Drug-like Small Molecules and Proteins. *Journal of Chemical Theory and Computation* **2016**, 12, 281–296, PMID: 26584231.

(33) Wang, L.; Friesner, R. A.; Berne, B. J. Replica Exchange with Solute Scaling: A More Efficient Version of Replica Exchange with Solute Tempering (REST2). *The Journal of Physical Chemistry B* **2011**, 115, 9431–9438, PMID: 21714551.

(34) Wang, L.; Wu, Y.; Deng, Y.; Kim, B.; Pierce, L.; Krilov, G.; Lupyan, D.; Robinson, S.; Dahlgren, M. K.; Greenwood, J. et al. Accurate and reliable prediction of relative ligand binding potency in prospective drug discovery by way of a modern free-energy calculation protocol and force field. *Journal of the American Chemical Society* **2015**, 137, 2695–2703.

(35) Ross, G. A.; Lu, C.; Scarabelli, G.; Albanese, S. K.; Houang, E.; Abel, R.; Harder, E. D.; Wang, L. The maximal and current accuracy of rigorous protein-ligand binding free energy calculations. *Communications Chemistry* **2023**, 6, 222.

(36) Azimi, S.; Khuttan, S.; Wu, J. Z.; Pal, R. K.; Gallicchio, E. Relative binding free energy calculations for ligands with diverse scaffolds with the alchemical transfer method. *Journal of Chemical Information and Modeling* **2022**, 62, 309–323.

(37) Schindler, C. E.; Baumann, H.; Blum, A.; Bose, D.; Buchstaller, H.-P.; Burgdorf, L.; Cappel, D.; Chekler, E.; Czodrowski, P.; Dorsch, D. et al. Large-scale assessment of binding free energy calculations in active drug discovery projects. *Journal of Chemical Information and Modeling* **2020**, 60, 5457–5474.

(38) York, D. M. Modern alchemical free energy methods for drug discovery explained. *ACS Physical Chemistry Au* **2023**, 3, 478–491.

(39) Ansari, N.; Jing, Z. F.; Gagelin, A.; Hédin, F.; Aviat, F.; Hénin, J.; Piquemal, J.-P.; Lagardère, L. Lambda-ABF-OPES: Faster Convergence with High Accuracy in Alchemical Free Energy Calculations. *The Journal of Physical Chemistry Letters* **2025**, 16, 4626–4634.

(40) Adjoua, O.; Lagardère, L.; Jolly, L.-H.; Durocher, A.; Very, T.; Dupays, I.; Wang, Z.; Inizan, T. J.; Célerse, F.; Ren, P. et al. Tinker-HP: Accelerating molecular dynamics simulations of large complex systems with advanced point dipole polarizable force fields using GPUs and multi-GPU systems. *J. Chem. Theory Comput.* **2021**, 17, 2034–2053.

(41) Hayes, R. L.; Buckner, J.; Brooks III, C. L. BLaDE: A basic lambda dynamics engine for GPU-accelerated molecular dynamics free energy calculations. *Journal of chemical theory and computation* **2021**, 17, 6799–6807.

(42) Blazhynska, M.; Ansari, N.; Lagardère, L.; Piquemal, J.-P. From Water Networks to Binding Affinities: Resolving Solvation Dynamics for Accurate Protein-Ligand Predictions. *bioRxiv* **2025**, 2025–10.

(43) Dalke, A.; Hastings, J. FMCS: a novel algorithm for the multiple MCS problem. 5, O6.

(44) Fiorin, G.; Marinelli, F.; Forrest, L. R.; Chen, H.; Chipot, C.; Kohlmeyer, A.; Santuz, H.; Hénin, J. Expanded functionality and portability for the Colvars library. *J. Phys. Chem. B* **2024**, 128, 11108–11123.

(45) Lagardère, L.; Jolly, L.-H.; Lipparini, F.; Aviat, F.; Stamm, B.; Jing, Z. F.; Harger, M.; Torabifard, H.; Cisneros, G. A.; Schnieders, M. J. et al. Tinker-HP: a massively parallel molecular dynamics package for multiscale simulations of large complex systems with advanced point dipole polarizable force fields. *Chem. Sci.* **2018**, 9, 956–972.

(46) Fiorin, G.; Klein, M. L.; Hénin, J. Using collective variables to drive molecular dynamics simulations. *Mol. Phys.* **2013**, 111, 3345–3362.

(47) Ponder, J. W.; Wu, C.; Ren, P.; Pande, V. S.; Chodera, J. D.; Schnieders, M. J.; Haque, I.; Mobley, D. L.; Lambrecht, D. S.; DiStasio Jr, R. A. et al. Current status of the AMOEBA polarizable force field. *J. Phys. Chem. B* **2010**, 114, 2549–2564.

(48) Wu, J. C.; Chattree, G.; Ren, P. Automation of AMOEBA polarizable force field parameterization for small molecules. *Theor. Chem. Acc.* **2012**, 131, 1–11.

(49) Shi, Y.; Xia, Z.; Zhang, J.; Best, R.; Wu, C.; Ponder, J. W.; Ren, P. Polarizable atomic multipole-based AMOEBA force field for proteins. *J. Chem. Theory Comput.* **2013**, 9, 4046–4063.

(50) Zhang, C.; Lu, C.; Jing, Z.; Wu, C.; Piquemal, J.-P.; Ponder, J. W.; Ren, P. AMOEBA polarizable atomic multipole force field for nucleic acids. *J. Chem. Theory Comput.* **2018**, 14, 2084–2108, PMID: 29438622.

(51) Walker, B.; Liu, C.; Wait, E.; Ren, P. Automation of AMOEBA polarizable force field for small molecules: Poltype 2. *J. Comput. Chem.* **2022**, 43, 1530–1542.

(52) Lagardère, L.; Aviat, F.; Piquemal, J.-P. Pushing the limits of multiple-time-step strategies for polarizable point dipole molecular dynamics. *J. Phys. Chem. Lett.* **2019**, 10, 2593–2599.

(53) Bussi, G.; Donadio, D.; Parrinello, M. Canonical sampling through velocity rescaling. *J. Chem. Phys.* **2007**, 126.

(54) Berendsen, H. J.; Postma, J. v.; Van Gunsteren, W. F.; DiNola, A.; Haak, J. R. Molecular dynamics with coupling to an external bath. *J. Chem. Phys.* **1984**, 81, 3684–3690.

(55) Essmann, U.; Perera, L.; Berkowitz, M. L.; Darden, T.; Lee, H.; Pedersen, L. G. A smooth particle mesh Ewald method. *J. Chem. Phys.* **1995**, 103, 8577–8593.

(56) Lagardère, L.; Lipparini, F.; Polack, E.; Stamm, B.; Cancès, E.; Schnieders, M.; Ren, P.; Maday, Y.; Piquemal, J.-P. Scalable evaluation of polarization energy and associated forces in polarizable molecular dynamics: II. Toward massively parallel computations using smooth particle mesh Ewald. *J. Chem. Theory Comput.* **2015**, 11, 2589–2599.

(57) Salari, R.; Joseph, T.; Lohia, R.; Hénin, J.; Brannigan, G. A Streamlined, general approach for computing ligand binding free energies and its application to GPCR-bound cholesterol. *J. Chem. Theory Comput.* **2018**, 14, 6560–6573.

(58) Baumann, H. M.; Dybeck, E.; McClendon, C. L.; Pickard IV, F. C.; Gapsys, V.; Pérez-Benito, L.; Hahn, D. F.; Tresadern, G.; Mathiowetz, A. M.; Mobley, D. L. Broadening the scope of binding free energy calculations using a separated topologies approach. *Journal of chemical theory and computation* **2023**, 19, 5058–5076.

(59) Liu, S.; Wu, Y.; Lin, T.; Abel, R.; Redmann, J. P.; Summa, C. M.; Jaber, V. R.; Lim, N. M.; Mobley, D. L. Lead optimization mapper: automating free energy calculations for lead optimization. *Journal of computer-aided molecular design* **2013**, 27, 755–770.

(60) Böttcher, J.; Dilworth, D.; Reiser, U.; Neumüller, R. A.; Schleicher, M.; Petronczki, M.; Zeeb, M.; Mischerikow, N.; Allali-Hassani, A.; Szewczyk, M. M. et al. Fragment-based discovery of a chemical probe for the PWWP1 domain of NSD3. *Nature chemical biology* **2019**, 15, 822–829.

(61) Alibay, I.; Magarkar, A.; Seeliger, D.; Biggin, P. C. Evaluating the use of absolute binding free energy in the fragment optimisation process. *Communications Chemistry* **2022**, 5, 105.

(62) Plé, T.; Adjoua, O.; Benali, A.; Posenitskiy, E.; Villot, C.; Lagardère, L.; Piquemal, J.-P. A foundation model for accurate atomistic simulations in drug design. **2025**,

Supplementary Information

for

“Fast, systematic and robust relative binding free energies for simple and complex transformations : DD-L-ABF-OPES”

Narjes Ansari,^{*,†} Félix Aviat,^{*,†} Jérôme Hénin,[‡] Jean-Philip Piquemal,^{†,¶} and Louis Lagardère^{*,†,¶}

[†]*Qubit Pharmaceuticals, 29 rue du Faubourg Saint Jacques, 75014 Paris, France*

[‡]*Laboratoire de Biochimie Théorique, UPR 9080 CNRS, Université de Paris Cité, 75005 Paris, France*

[¶]*Laboratoire de Chimie Théorique, Sorbonne Université, UMR 7616 CNRS, 75005 Paris, France*

E-mail: narjesa@qubit-pharmaceuticals.com; felix.aviat@qubit-pharmaceuticals.com;
louis.lagardere@sorbonne-universite.fr

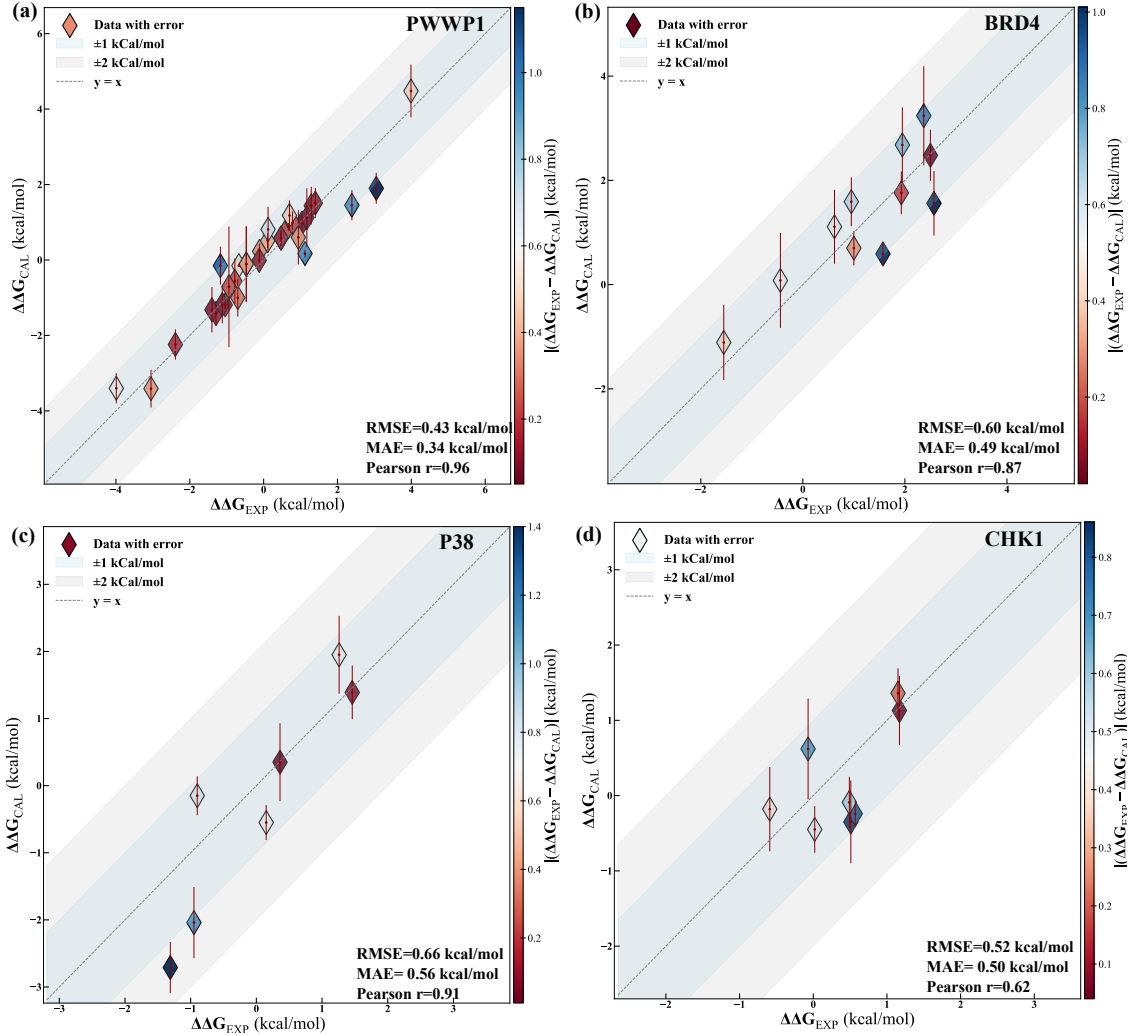


Figure S1: Experimental vs. Calculated Relative Binding Free Energy Changes ($\Delta\Delta G$). (a) PWWP1, (b) BRD4, (c) P38, and (d) CHK1 complexes. The calculated $\Delta\Delta G$ values from RBFE results and associated errors represent the mean \pm standard error from three independent repeats. The dark and light shaded regions indicate ± 1 kcal/mol and ± 2 kcal/mol deviations, respectively. The color bar displays the absolute difference between the experimental and computed values, $|\Delta\Delta G_{\text{EXP}} - \Delta\Delta G_{\text{CAL}}|$. For each system, Pearson's r , RMSE, and MAE statistics are reported.

PWWP1

Fig. S2 represents the 2D structures of the 12 ligands studied for PWWP1.

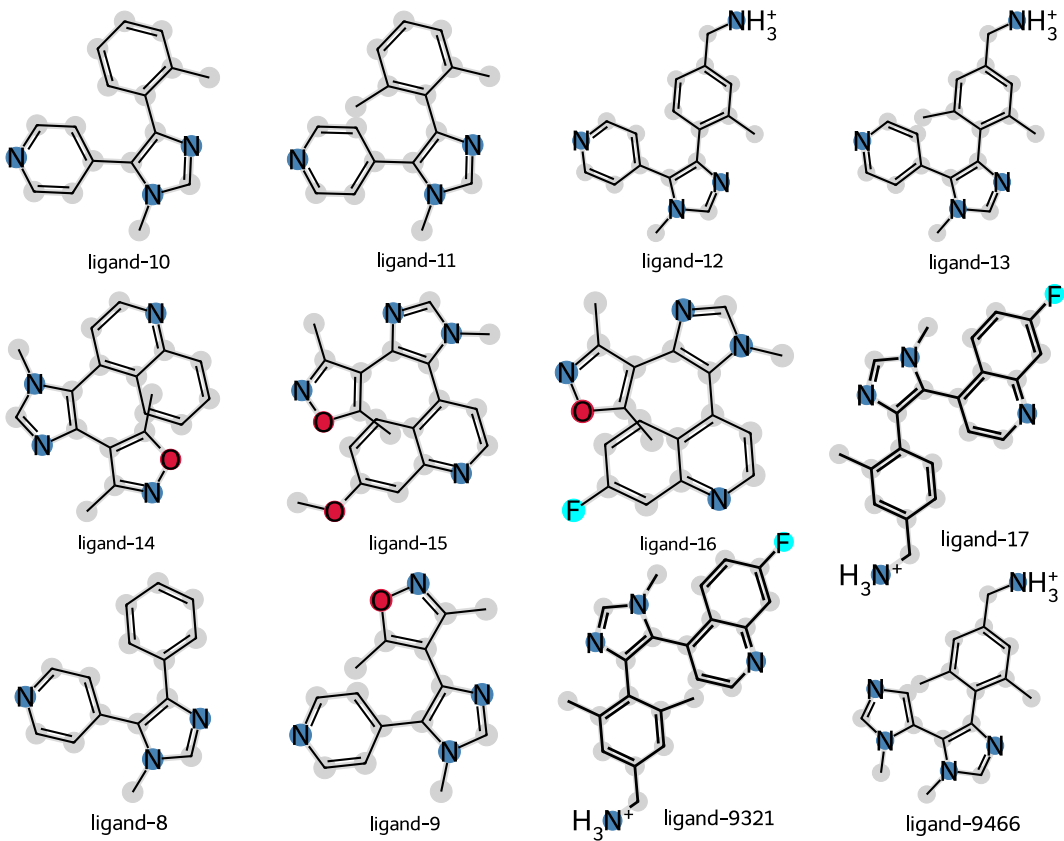


Figure S2: 2D structures of all ligands complexed with PWWP1.

PMF evolution in .hist.pmf files

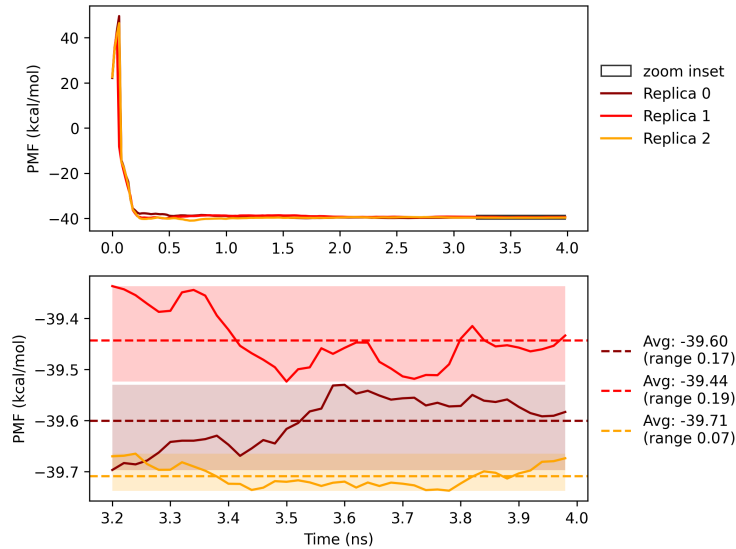


Figure S3: Convergence plot of the Potential of Mean Force (PMF) for the complex phase of the ligand 10 to ligand 12 transformation in PWWP1.

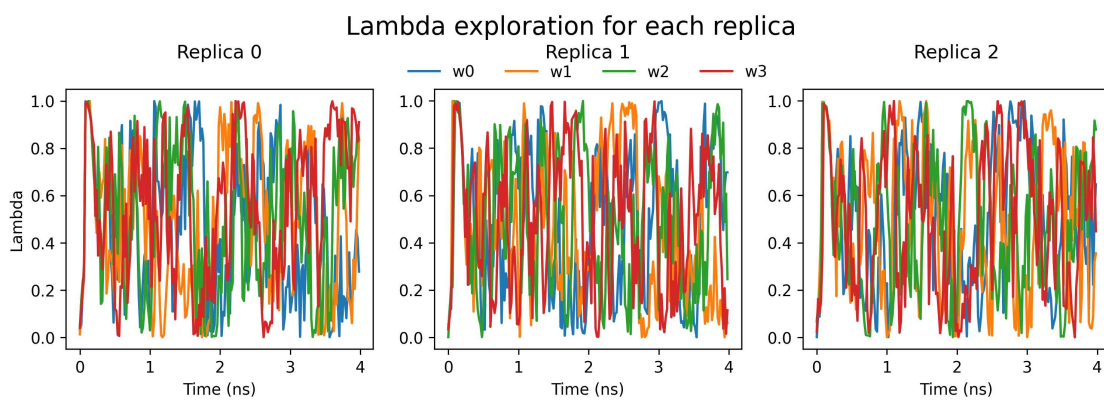


Figure S4: Lambda fluctuation over time for the complex phase of the ligand 10 to ligand 12 transformation in PWWP1.

PMF evolution in .hist.pmf files

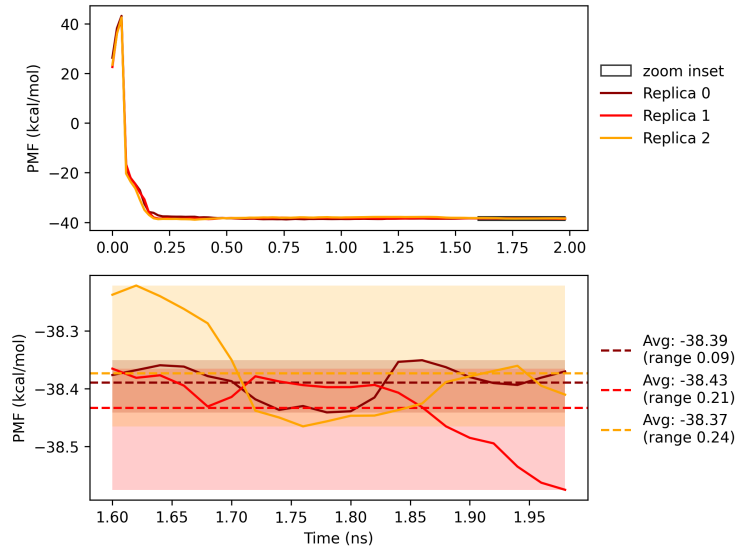


Figure S5: Convergence plot of the Potential of Mean Force (PMF) for the solvent phase of the ligand 10 to ligand 12 transformation in PWWP1.

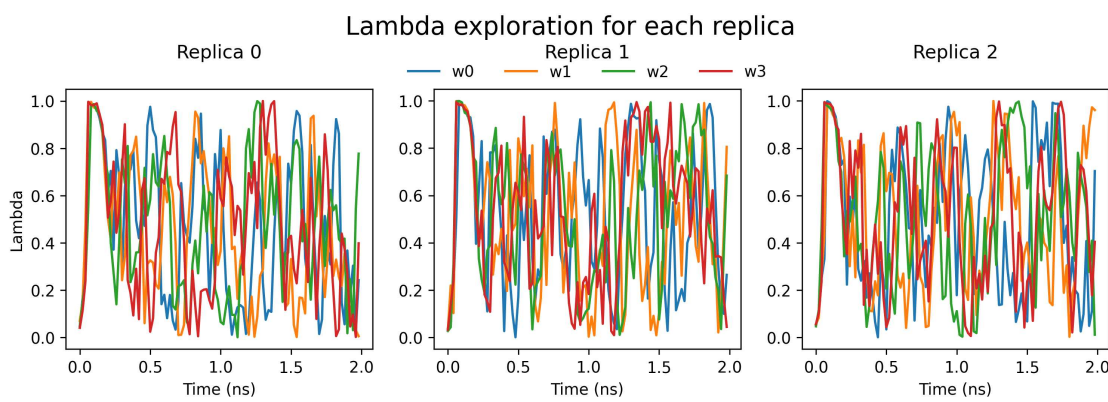


Figure S6: Lambda fluctuation over time for the solvent phase of the ligand 10 to ligand 12 transformation in PWWP1.

Table S1: **Relative Binding Free Energy ($\Delta\Delta G$) Results for PWWP1 Side-Chain Transformations.** Comparison of experimental ($\Delta\Delta G_{\text{EXP}}$) and calculated ($\Delta\Delta G_{\text{CAL}}$) relative binding free energies for the PWWP1 set. All $\Delta\Delta G_{\text{CAL}}$ values and their associated standard deviations ($\pm \text{std}$) are reported in kcal/mol. The error is calculated as $\Delta\Delta G_{\text{CAL}} - \Delta\Delta G_{\text{EXP}}$.

pairs	$\Delta\Delta G_{\text{EXP}}^1$	$\Delta\Delta G_{\text{CAL}} \pm \text{std}$	Dual-DBC error
Lig10tolig11	-0.11	0.23 ± 0.22	-0.34
Lig11tolig10	0.11	0.51 ± 0.15	-0.40
Lig10tolig12	-1.04	-1.19 ± 0.14	0.15
Lig12tolig10	1.04	0.98 ± 0.16	0.06
lig10tolig8	1.29	1.44 ± 0.48	-0.15
Lig8tolig10	-1.29	-1.42 ± 0.30	0.13
Lig10tolig9	0.12	0.81 ± 0.63	-0.69
Lig9tolig10	-0.12	-0.01 ± 0.17	-0.11
Lig11tolig8	1.4	1.51 ± 0.36	-0.11
Lig8tolig11	-1.40	-1.32 ± 0.59	-0.08
Lig12tolig13	0.67	0.88 ± 0.10	-0.21
Lig13tolig12	-0.67	-0.15 ± 0.04	-0.52
Lig12tolig17	-0.78	-0.56 ± 0.62	-0.22
Lig17tolig12	0.78	0.99 ± 0.32	-0.21
Lig13tolig9321	-2.39	-2.24 ± 0.41	-0.15
Lig9321tolig13	2.39	1.45 ± 0.40	0.94
Lig9tolig14	-0.47	-0.11 ± 0.97	-0.36
Lig14tolig9	0.47	0.58 ± 0.17	-0.11
Lig15tolig16	-1.12	-1.18 ± 0.51	0.06

BRD4

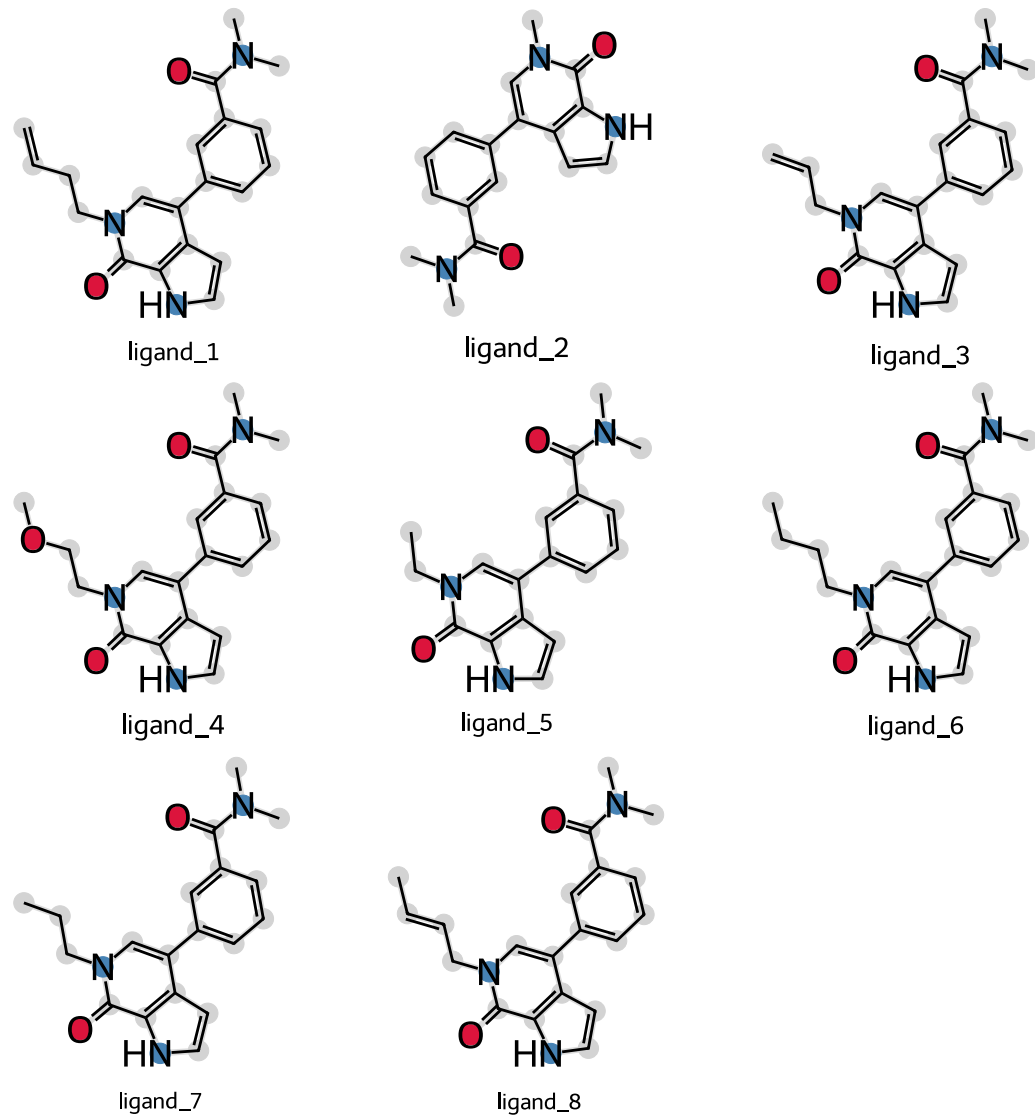


Figure S7: 2D structures of all ligands complexed with BRD4.

Table S2: **Relative Binding Free Energy ($\Delta\Delta G$) Results for BRD4.** Comparison of experimental ($\Delta\Delta G_{\text{EXP}}$) and calculated ($\Delta\Delta G_{\text{CAL}}$) relative binding free energies for the BRD4 set. All $\Delta\Delta G_{\text{CAL}}$ values and their associated standard deviations ($\pm \text{std}$) are reported in kcal/mol.

Ligand	$\Delta\Delta G_{\text{EXP}}$	$\Delta\Delta G_{\text{CAL}} \pm \text{std}$
Lig2tolig3	2.5	2.48 ± 0.49
Lig2tolig4	0.95	1.59 ± 0.47
Lig2tolig1	1.95	2.68 ± 0.72
Lig2tolig6	1	0.70 ± 0.33
Lig2tolig7	2.57	1.56 ± 0.62
Lig2tolig8	1.93	1.76 ± 0.41
Lig2tolig9	2.37	3.24 ± 0.95
Lig3tolig4	-1.55	-1.11 ± 0.72
Lig5tolig7	0.62	1.11 ± 0.71
Lig6tolig7	1.57	0.59 ± 0.21
Lig9tolig8	-0.44	0.08 ± 0.91

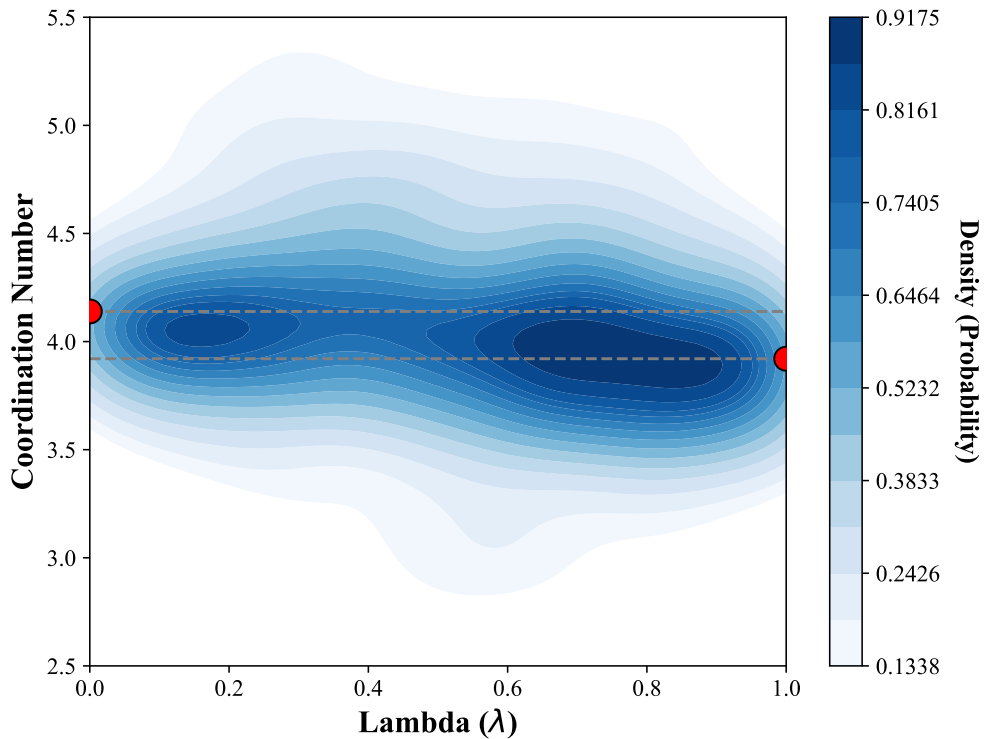


Figure S8: Density Plot of Water Coordination Number around Ligand O1 Atom During Alchemical Transformation. The plot shows the density distribution of the coordination number (CN) of water molecules around the O1 atom of ligand 2 as a function of the alchemical coupling parameter, λ , for the ligand 2 \rightarrow ligand 5 transformation. Water oxygen atoms (O_{water}) were counted within a cutoff distance of 5 Å from the O1 atom of the transforming ligand. The red circles mark the average coordination numbers at the end states: $\lambda = 0$ (representing ligand 2) and $\lambda = 1$ (representing ligand 5). The corresponding dashed lines indicate these average coordination number values, which slightly decrease as the system transforms from ligand 2 to ligand 5.

PMF evolution in .hist.pmf files

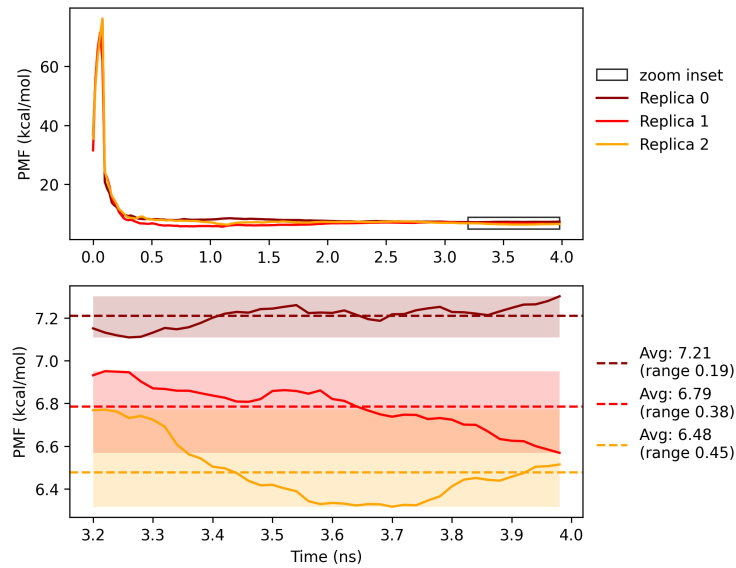


Figure S9: Convergence plot of the Potential of Mean Force (PMF) for the complex phase of the ligand 2 to ligand 8 transformation in BRD4.

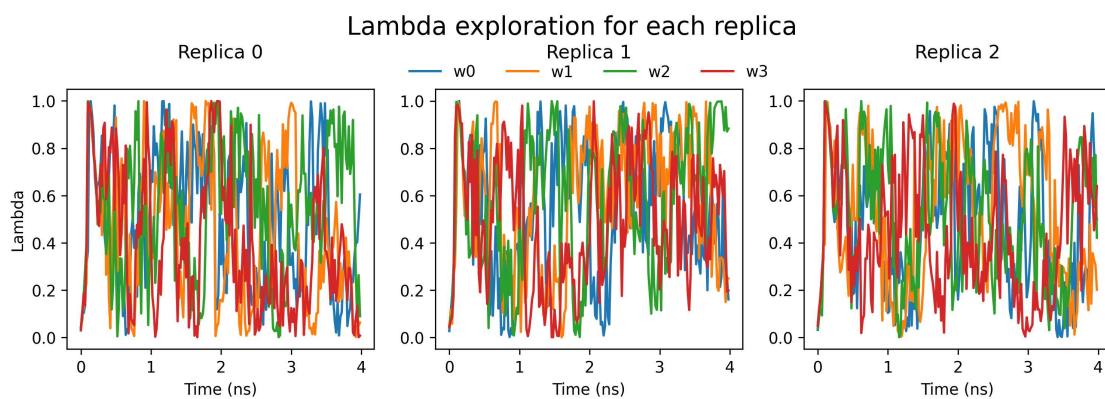


Figure S10: Lambda fluctuation over time for the complex phase of the ligand 2 to ligand 8 transformation in BRD4.

PMF evolution in .hist.pmf files

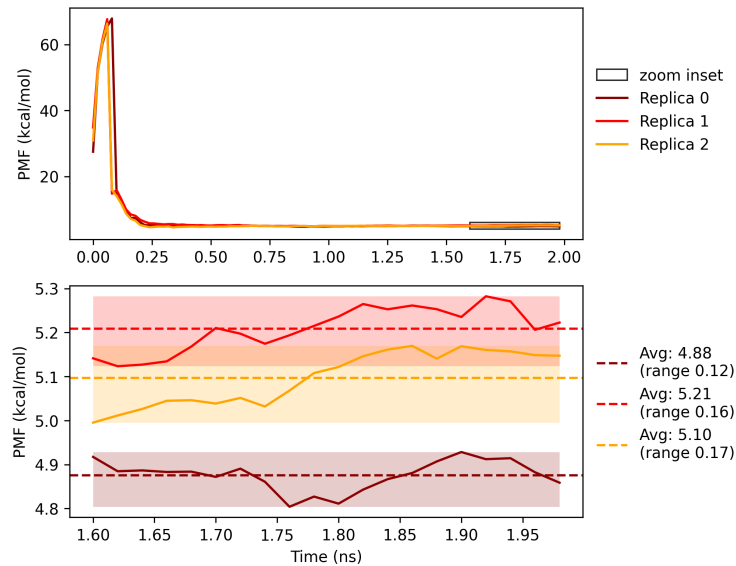


Figure S11: **Convergence plot of the Potential of Mean Force (PMF) for the solvent phase of the ligand 2 to ligand 8 transformation in BRD4.**

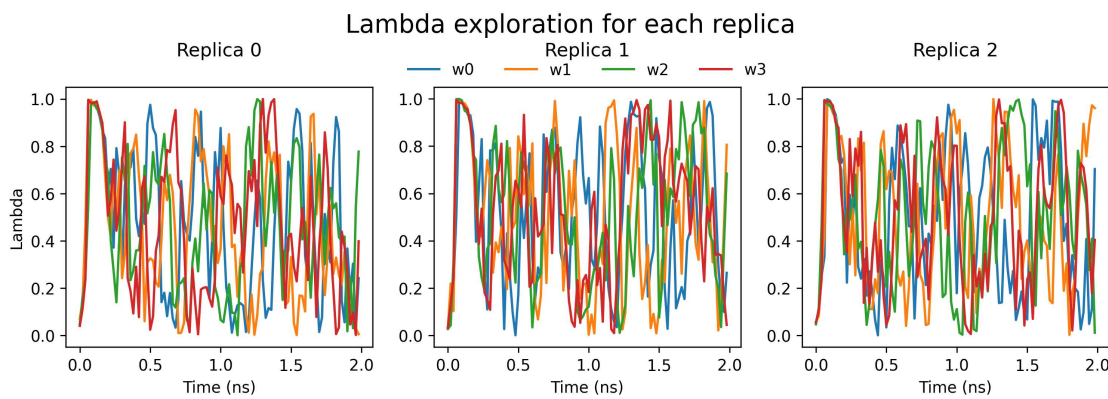


Figure S12: **Lambda fluctuation over time for the solvent phase of the ligand 10 to ligand 12 transformation.**

P38

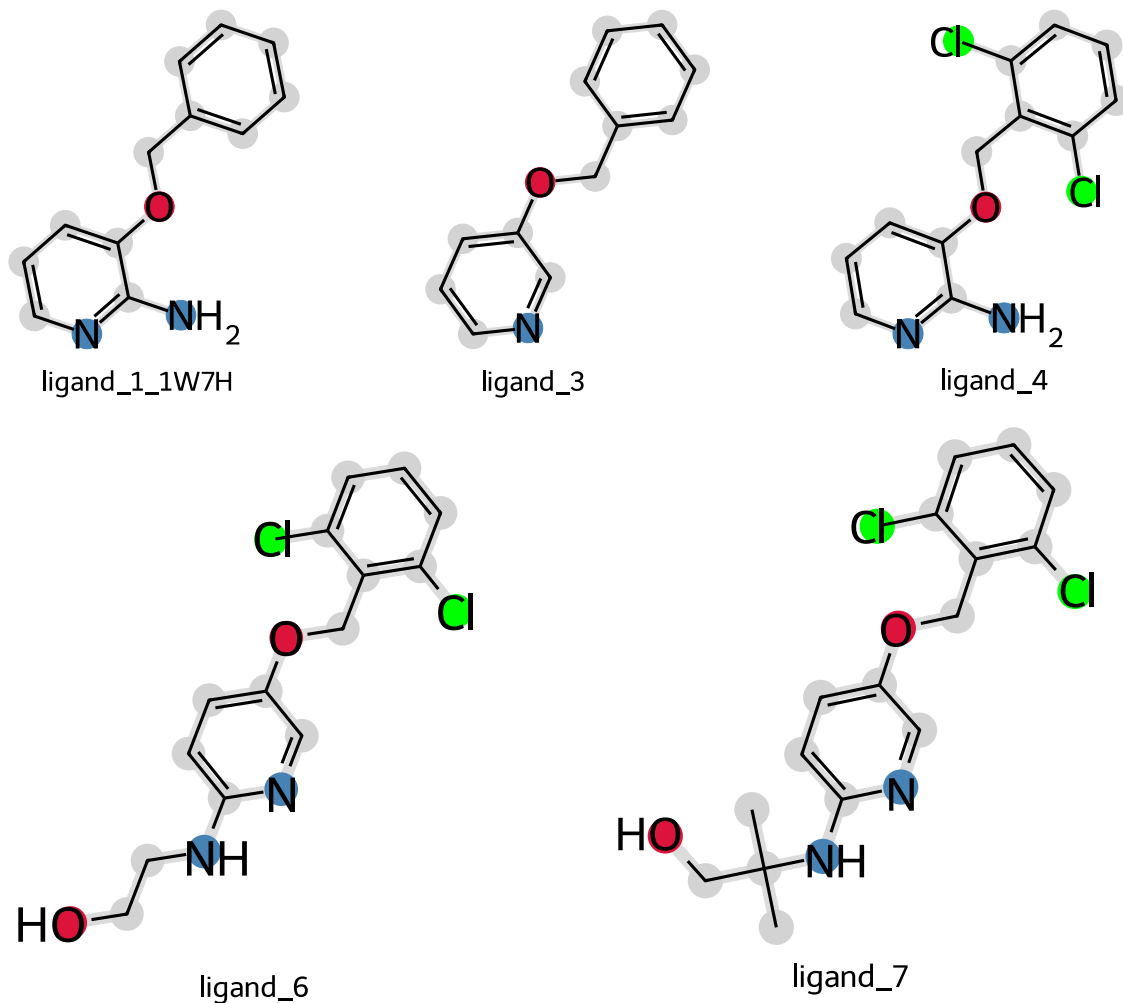


Figure S13: **2D structures of all ligands complexed with P38.**

Table S3: **Relative Binding Free Energy ($\Delta\Delta G$) Results for P38.** Comparison of experimental ($\Delta\Delta G_{\text{EXP}}$) and calculated ($\Delta\Delta G_{\text{CAL}}$) relative binding free energies for the P38 set. All $\Delta\Delta G_{\text{CAL}}$ values and their associated standard deviations ($\pm \text{std}$) are reported in kcal/mol.

Ligand	$\Delta\Delta G_{\text{EXP}}$	$\Delta\Delta G_{\text{CAL}} \pm \text{std}$
lig4tolig1	1.46	1.39 ± 0.40
lig4tolig7	-0.9	-0.15 ± 0.29
lig3tolig4	-1.31	-2.71 ± 0.38
lig4tolig6	0.36	0.35 ± 0.58
lig3tolig1	0.15	-0.55 ± 0.26
lig7tolig6	1.26	1.95 ± 0.58
lig3tolig6	-0.95	-2.04 ± 0.53

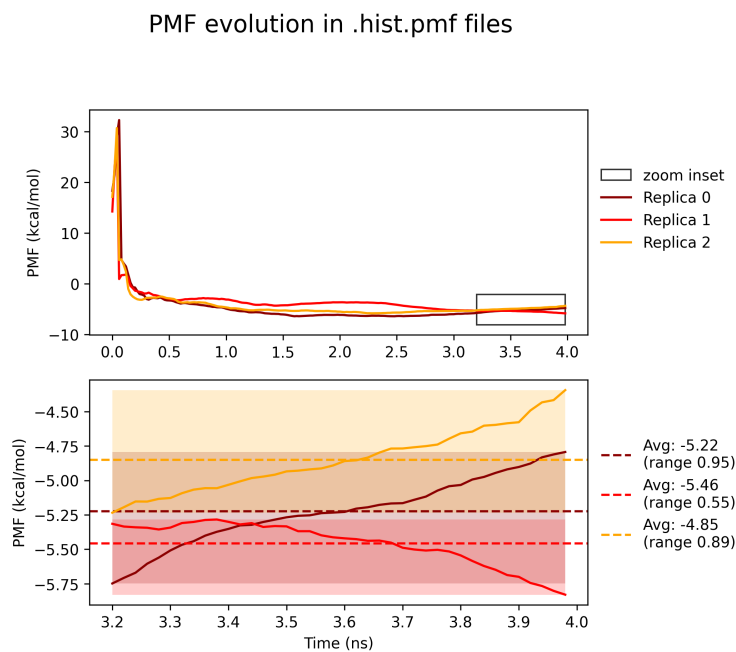


Figure S14: **Convergence plot of the Potential of Mean Force (PMF) for the complex phase of the ligand 4 to ligand 7 transformation in P38.**

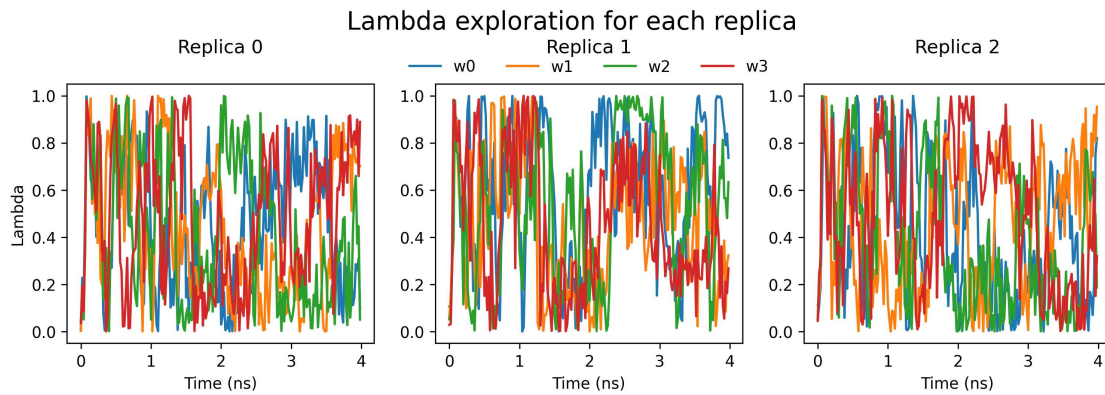


Figure S15: Lambda fluctuation over time for the complex phase of the ligand 4 to ligand 7 transformation in P38.

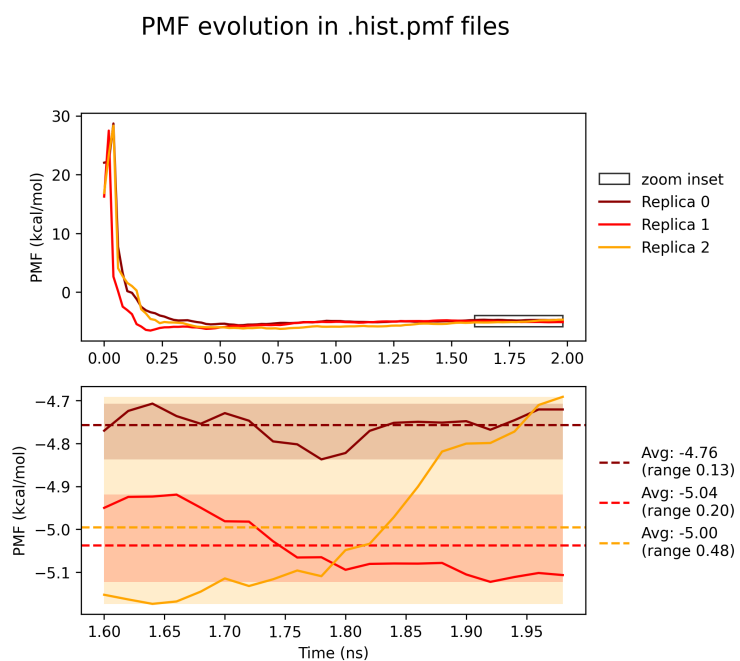


Figure S16: Convergence plot of the Potential of Mean Force (PMF) for the solvent phase of the ligand 4 to ligand 7 transformation in P38.

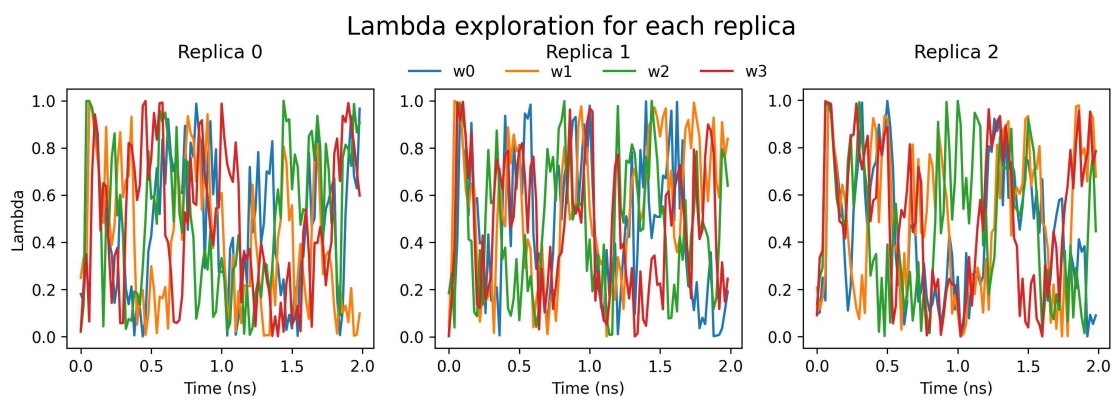


Figure S17: Lambda fluctuation over time for the solvent phase of the ligand 4 to ligand 7 transformation in P38.

CHK1

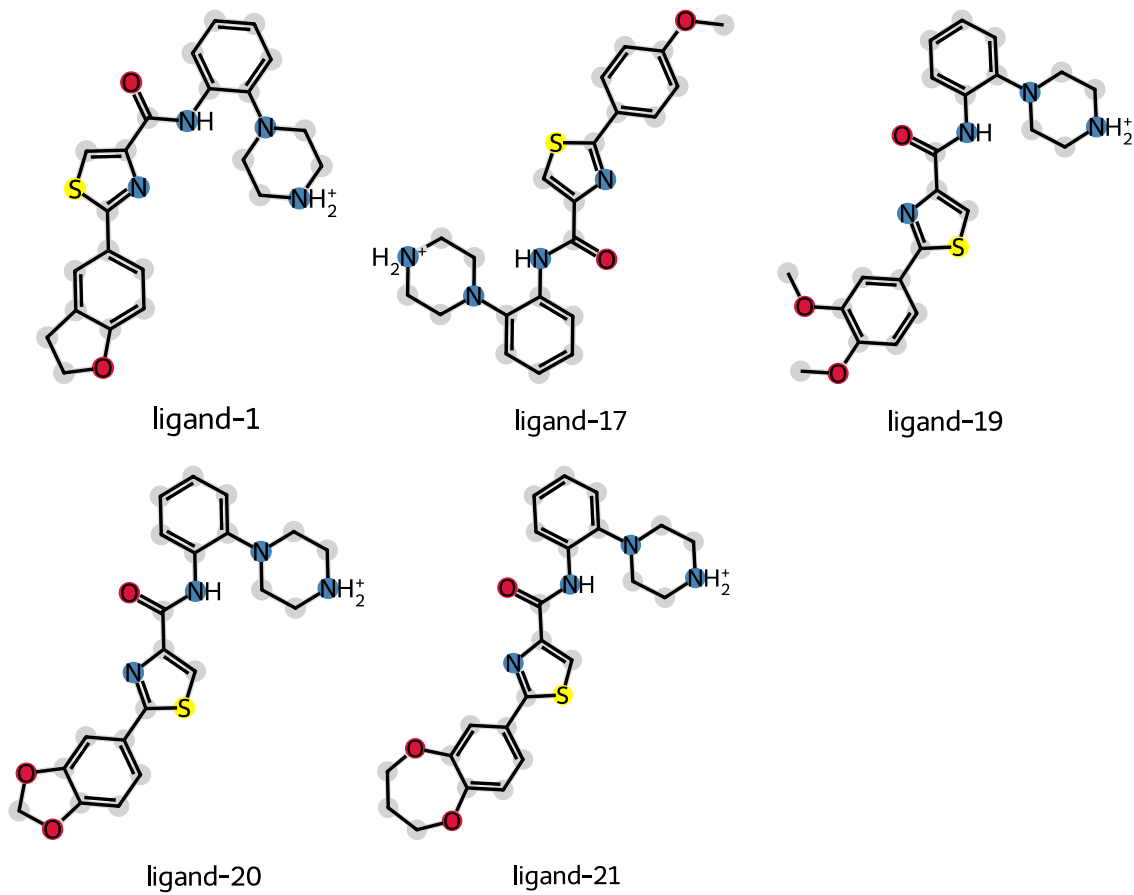


Figure S18: 2D structures of all ligands complexed with CHK1.

Table S4: **Relative Binding Free Energy ($\Delta\Delta G$) Results for CHK1.** Comparison of experimental ($\Delta\Delta G_{\text{EXP}}$) and calculated ($\Delta\Delta G_{\text{CAL}}$) relative binding free energies for the CHK1 set. All $\Delta\Delta G_{\text{CAL}}$ values and their associated standard deviations ($\pm \text{std}$) are reported in kcal/mol.

Ligand	$\Delta\Delta G_{\text{EXP}}$	$\Delta\Delta G_{\text{CAL}} \pm \text{std}$
lig17tolig1	0.02	-0.45 \pm 0.31
lig17tolig19	1.17	1.13 \pm 0.46
lig17tolig20	0.51	-0.35 \pm 0.55
lig17tolig21	0.57	-0.24 \pm 0.17
lig1tolig19	1.15	1.36 \pm 0.33
lig1tolig20	0.49	-0.09 \pm 0.34
lig19tolig21	-0.59	-0.18 \pm 0.56
lig21tolig20	-0.07	0.62 \pm 0.67

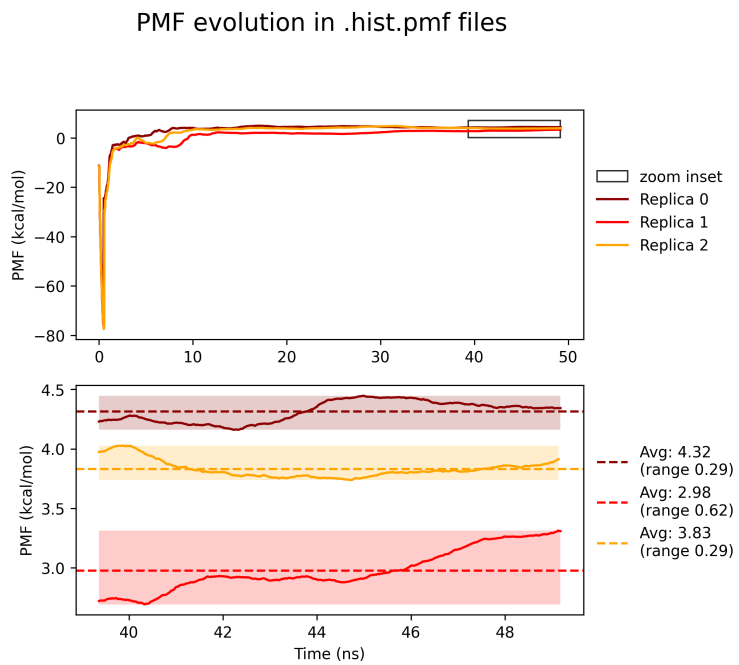


Figure S19: **Convergence plot of the Potential of Mean Force (PMF) for the complex phase of the ligand 19 to ligand 21 transformation in CHK1.**

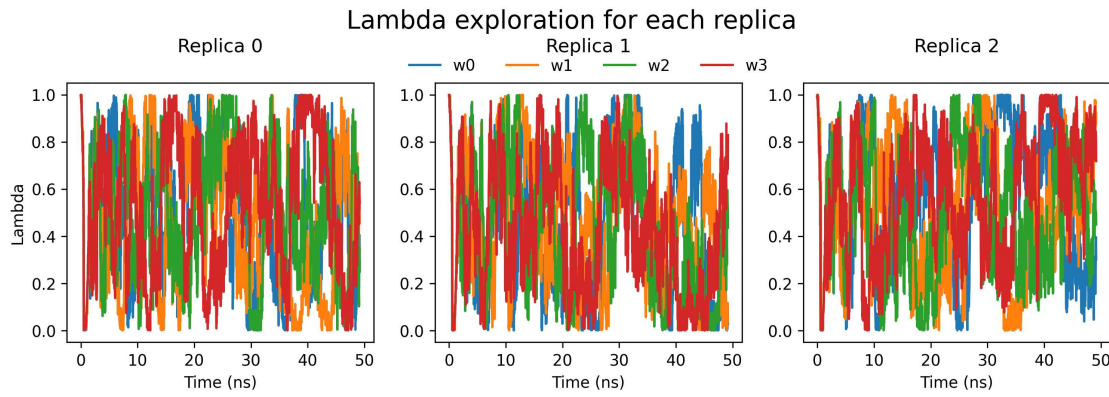


Figure S20: Lambda fluctuation over time for the complex phase of the ligand 19 to ligand 21 transformation in CHK1.

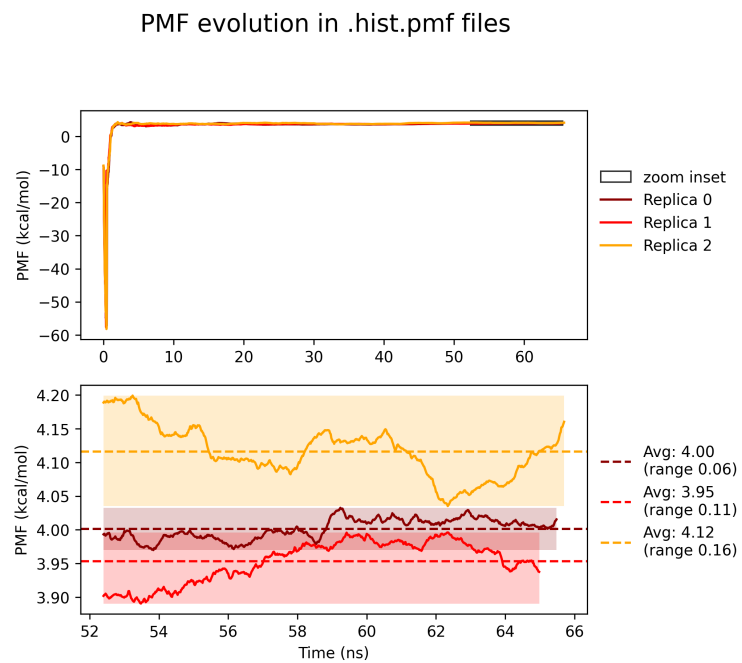


Figure S21: Convergence plot of the Potential of Mean Force (PMF) for the solvent phase of the ligand 19 to ligand 21 transformation in CHK1.

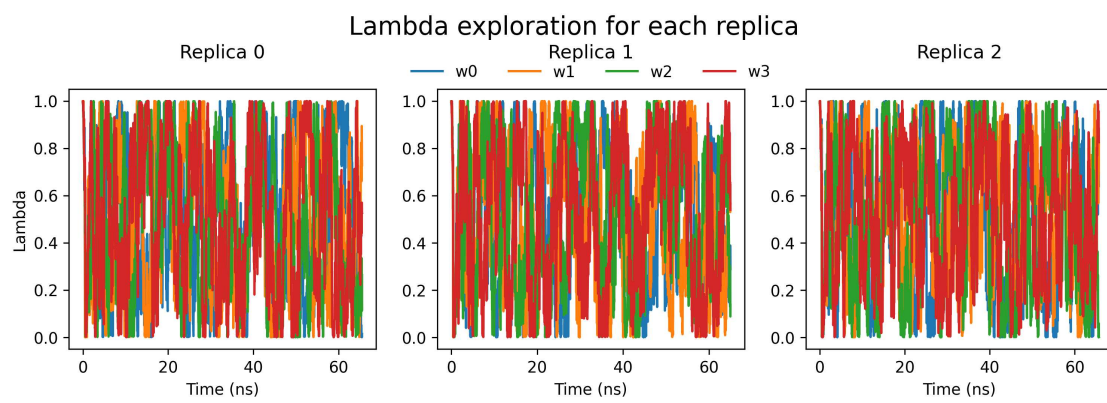


Figure S22: Lambda fluctuation over time for the solvent phase of the ligand 19 to ligand 21 transformation in CHK1.

BEN - Multisite simulations

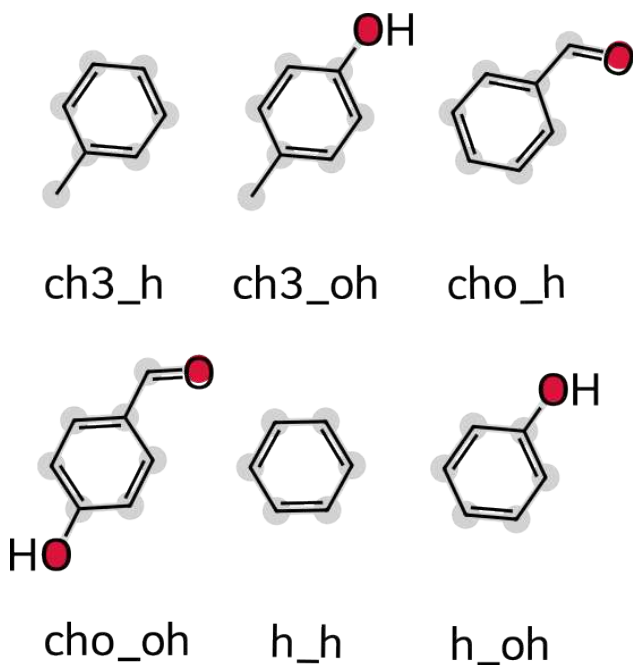


Figure S23: **2D structures of all benzene derivatives for which Hydration Free Energies were computed.** Ligand names are composed of the substituents carried by the benzene cycle, separated by an underscore symbol ("h_h" designates benzene, "h_oh" toluene, *etc.*).

Table S5: **Relative hydration free energies for a family of benzene-derivated compounds.** Columns "Dual" and "Multi" report the relative hydration free energies obtained using a dual- and multiple-topology scheme, respectively. All quantities reported in kcal/mol. "std" denotes the standard deviation computed on three replicas. Ligand names are composed of the substituents carried by the benzene cycle, separated by an underscore symbol ("h_h" designates benzene, "h_oh" toluene, *etc.*).

Ligand 1	Ligand 2	$\Delta\Delta G_{\text{dual}} \pm \text{std}$	$\Delta\Delta G_{\text{multi}} \pm \text{std}$
h_h	h_oh	-4.44 \pm 0.03	-4.56 \pm 0.17
h_h	ch3_h	0.18 \pm 0.07	0.24 \pm 0.02
h_h	ch3_oh	-4.32 \pm 0.12	-4.32 \pm 0.07
h_h	cho_h	-2.31 \pm 0.07	-2.12 \pm 0.10
h_h	cho_oh	-7.48 \pm 0.12	-7.43 \pm 0.11
h_oh	ch3_h	4.70 \pm 0.07	4.68 \pm 0.07
h_oh	ch3_oh	0.17 \pm 0.09	0.15 \pm 0.13
h_oh	cho_h	2.22 \pm 0.02	2.16 \pm 0.05
h_oh	cho_oh	-2.96 \pm 0.38	-3.18 \pm 0.36
ch3_h	ch3_oh	-4.56 \pm 0.09	-4.39 \pm 0.10
ch3_h	cho_h	-2.40 \pm 0.09	-2.41 \pm 0.05
ch3_h	cho_oh	-7.84 \pm 0.05	-7.77 \pm 0.32
ch3_oh	cho_h	2.03 \pm 0.13	2.11 \pm 0.15
ch3_oh	cho_oh	-3.16 \pm 0.24	-3.62 \pm 0.31
cho_h	cho_oh	-4.90 \pm 0.25	-5.49 \pm 0.21

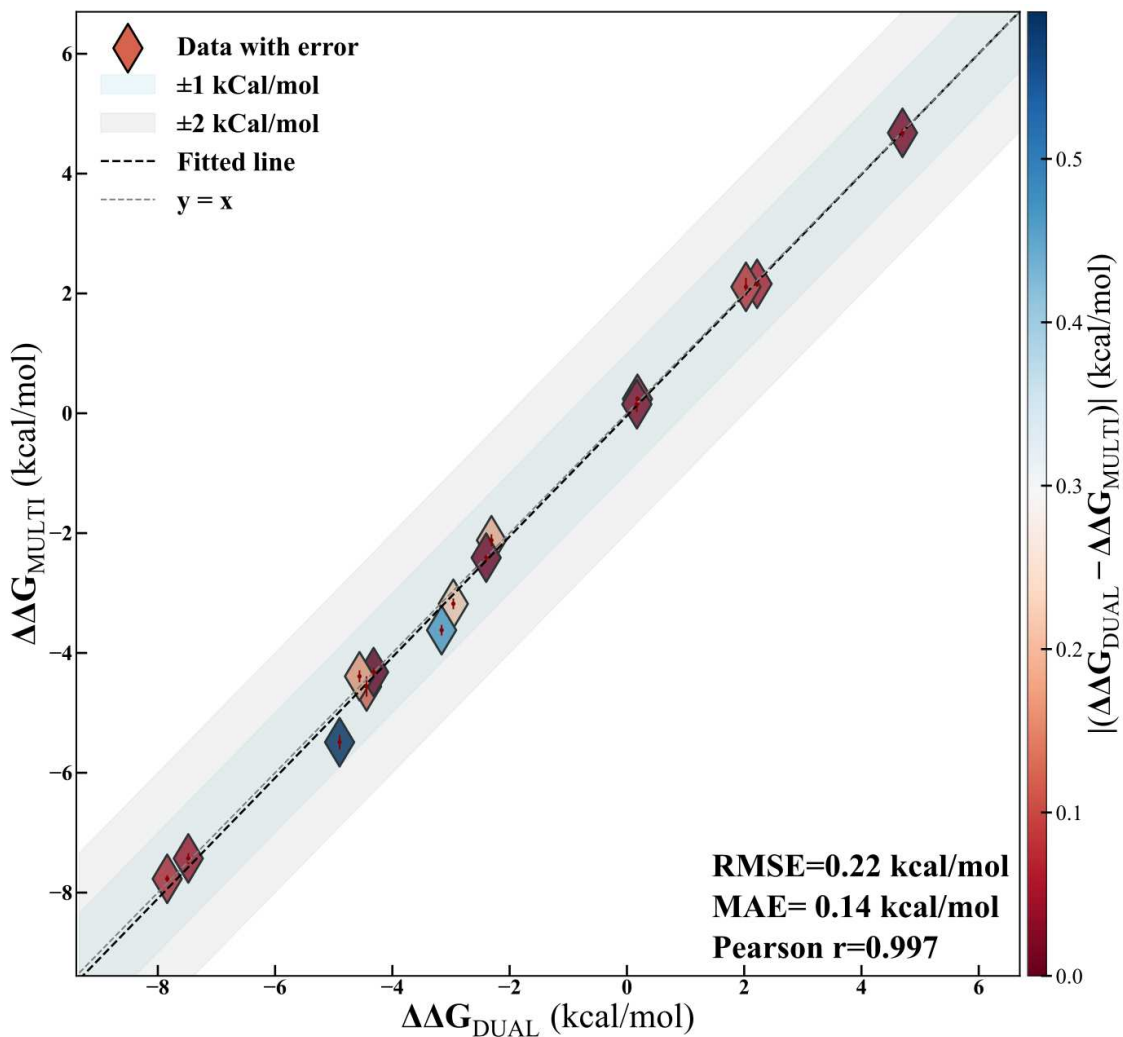


Figure S24: **Hydration Free Energies computed using the Multiple vs. Dual topology approaches**, on the 15 pairs built from the six molecules presented above. Error bars represent the standard deviation obtained from three independent repeats. Points are colored depending on the absolute error between values obtained with the dual and multiple topology approaches.

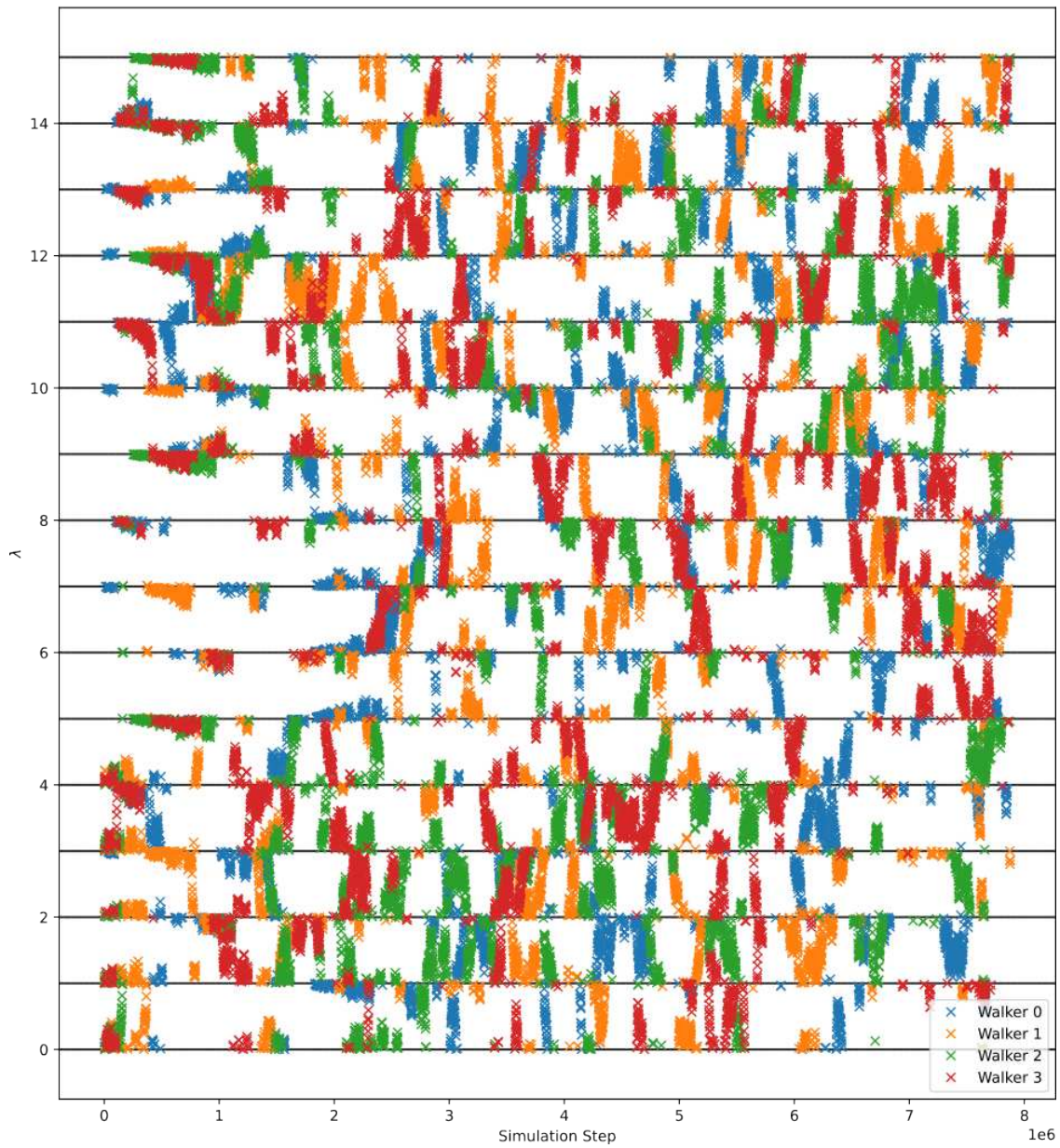


Figure S25: **Lambda fluctuation over time** for the solvent phase simulation of one replica, in the case of the multiple topology calculation of hydration free energies. Each color designates a different walker. Timestep used was 2 fs.

Each λ subdivision of length 1 ($[0; 1]$, $[1; 2]$, etc.) shows the exploration along an edge of the graph.

Calculation of ABFE (ΔG) from RBFE ($\Delta\Delta G$)

The Absolute Binding Free Energies (ΔG) for the series of ligands presented are derived from the calculated Relative Binding Free Energies ($\Delta\Delta G$) using a statistical method called "Weighted Least-Squares Fitting" of the RBFE network.²

Weighted Least-Squares Fitting

The set of calculated $\Delta\Delta G$ values constitutes an **overdetermined system** of linear equations. The fitting procedure finds the single set of ΔG values for all ligands (L_i) that minimizes the sum of squared residuals (RMSE) across all calculated transformations ($\Delta\Delta G_{i \rightarrow j}^{\text{calc}}$):

$$\text{Minimize} \sum_{i \rightarrow j} w_{i \rightarrow j} [(\Delta G_{L_j} - \Delta G_{L_i}) - \Delta\Delta G_{i \rightarrow j}^{\text{calc}}]^2$$

The minimization is weighted ($w_{i \rightarrow j}$) by the inverse variance of the calculated $\Delta\Delta G$ values ($w \propto 1/\sigma^2$). This weighting ensures that the most precise $\Delta\Delta G$ calculations (those with the smallest statistical uncertainty) contribute most significantly to the final fitted ΔG values.

Anchoring and Final Results

The least-squares fit initially yields a relative set of ΔG values (ΔG^{rel}). To place these results onto the experimental scale, the entire network is shifted by aligning the ΔG^{rel} values to the corresponding experimental ΔG^{exp} data for all available ligands. The final reported ΔG values represent the statistically most probable and thermodynamically consistent binding free energies derived from the calculated RBFE network, along with the rigorously propagated statistical uncertainty.

References

- (1) Böttcher, J.; Dilworth, D.; Reiser, U.; Neumüller, R. A.; Schleicher, M.; Petronczki, M.; Zeeb, M.; Mischerikow, N.; Allali-Hassani, A.; Szewczyk, M. M.; others Fragment-based discovery of a chemical probe for the PWWP1 domain of NSD3. *Nature chemical biology* **2019**, *15*, 822–829.
- (2) Wang, L.; Wu, Y.; Deng, Y.; Kim, B.; Pierce, L.; Krilov, G.; Lupyan, D.; Robinson, S.; Dahlgren, M. K.; Greenwood, J.; others Accurate and reliable prediction of relative ligand binding potency in prospective drug discovery by way of a modern free-energy calculation protocol and force field. *Journal of the American Chemical Society* **2015**, *137*, 2695–2703.